17221

c1

# A MAGNETICALLY STABILIZED HELIUM ARC FOR SCATTERING EXPERIMENTS

by

VINKO POTOČNIK

Dipl. Eng. Phys., University of Ljubljana,
Yugoslavia, 1967

A THESIS SUBMITTED IN PARTIAL FULFILLMENT OF
THE REQUIREMENTS FOR THE DEGREE OF
DOCTOR OF PHILOSOPHY

in the Department
of
PHYSICS

We accept this thesis as conforming to the
required standard

THE UNIVERSITY OF BRITISH COLUMBIA

July, 1973

In presenting this thesis in partial fulfilment of the requirements for an advanced degree at the University of British Columbia, I agree that the Library shall make it freely available for reference and study. I further agree that permission for extensive copying of this thesis for scholarly purposes may be granted by the Head of my Department or by his representatives. It is understood that copying or publication of this thesis for financial gain shall not be allowed without my written permission.

Department of Physics

The University of British Columbia
Vancouver 8, Canada

Date Sept. 19, 1973

# ABSTRACT

For verifying some theoretical predictions of light scattering from magnetized plasmas, a stable pulsed helium arc discharge in a magnetic field up to 5 Teslas has been built. The arc has been investigated at filling pressures of 2 to 5 torr and plasma currents between 1 and 5 kA. Plasma parameters were measured at a magnetic field of 4 Teslas and a pressure of 3 torr. At these values of the magnetic field and the filling pressure the arc is steady and approximately cylindrically symmetric up to a plasma current of 2.8 kA.

Time dependence and radial distribution of the electron density and temperature have been determined from spectroscopic measurements, laser interferometry, and laser scattering. The latter two techniques were used successfully for the first time on a magnetically stabilized arc to measure the electron density and temperature in the hot core of the arc. The axial electron density is $1.2 \times 10^{16}$ $cm^{-3}$ and is approximately constant over the arc cross-section in the high temperature region as predicted by theory. The axial temperature is 145,000 $^{o}K$. Thus the arc design and the plasma properties are suitable for scattering experiments.

The arc behaviour is governed by dynamic processes which depend on the geometry of the apparatus. In order to show the problems of the design and operation of the apparatus, the theory of arc behaviour in a magnetic field is outlined.

# TABLE OF CONTENTS

Page

ABSTRACT . . . . . ii

TABLE OF CONTENTS . . . . . iii

LIST OF FIGURES . . . . . vii

ACKNOWLEDGEMENT . . . . . ix

INTRODUCTION . . . . . 1

Chapter

1. THEORY OF ELECTRIC ARC IN A LONGITUDINAL MAGNETIC FIELD . . . . . 4

1.1 Pressure Increase . . . . . 6

1.1.1 Thermomagnetic or Nernst Effect . . . . . 13

1.1.2 Ambipolar Diffusion . . . . . 15

1.1.3 Pinch Effect . . . . . 16

1.1.4 Hall Effect . . . . . 16

1.1.5 Mass Currents in the Arc . . . . . 17

1.2 Distribution of the Electric Current, Electric Field and Arc Rotation . . . . 19

1.3 Unstationary States of the Arc . . . . . 21

2. DESIGN OF THE APPARATUS . . . . . 25

2.1 Production of High Magnetic Field . . . . . 25

2.2 Discharge Design . . . . . 30

2.2.1 Discharge Tube . . . . . 30

2.2.2 Plasma Current, Filling Pressure, Timing . . . . . 33

Chapter Page

3. TIME RESOLVED SPECTROSCOPY . . . . . 36

3.1 Theory . . . . . 37

3.1.1 Abel Unfolding of Spectral Lines . . . . . 38

3.1.2 Spectral Line Broadening and the Electron Density . . . . . 40

3.1.2.1 Broadening of He I 4471 Å. 41

3.1.3 Line Intensity Ratio and the Electron Temperature . . . . . 45

3.1.3.1 Static (Corona) Ionization Ratio $n_Z/n_{Z-1}$ . . . 46

3.1.3.2 Dynamic Ionization Ratio $n_Z/n_{Z-1}$ . . . . . 48

3.2 Experiment . . . . . 53

3.2.1 Optical System . . . . . 53

3.2.2 Plate Analysis . . . . . 58

3.2.3 Interpretation of Spectral Line Intensities . . . . . 60

3.2.4 Photographic Study of the Arc . . 62

4. LASER INTERFEROMETRY . . . . . 63

4.1 Theory . . . . . 63

4.2 Experiment . . . . . 65

4.3 Interpretation of Interferograms . . . . 67

4.3.1 Plasma Homogeneity . . . . . 67

4.3.2 Instability of Fringes Due to Unstationary Behaviour of Plasma . . . . . 68

4.3.3 The Ambiguity of the Final (Initial) Phase . . . . . 70

Chapter Page

4.3.4 Sign of the Time Derivative of the Electron Density . . . . . 70

5. LASER SCATTERING . . . . . 72

5.1 Theory . . . . . 72

5.1.1 Scattered Power and Spectral Distribution . . . . . 72

5.1.2 Fitting of Experimental Data to the Theoretical Profiles . . . . 76

5.2 Experiment . . . . . 79

5.2.1 Scattering Apparatus . . . . . 80

5.2.1.1 Description . . . . . 80

5.2.1.2 Alignment . . . . . 85

5.2.1.3 Experimental Procedure . . . . . 86

6. RESULTS AND DISCUSSION . . . . . 87

6.1 Results . . . . . 87

6.1.1 Photographic Study of the Arc . . . . . 87

6.1.2 Radial Distribution of the Electron Density . . . . . 95

6.1.3 Radial Distribution of Electron Temperature . . . . . 99

6.2 Discussion . . . . . 101

6.2.1 Arc Rotation . . . . . 101

6.2.2 Electron Density Distribution . . 103

6.2.3 Electron Temperature Distribution . . . . . 105

6.2.4 Ion Temperature . . . . . 106

Chapter Page

6.2.5 Pressure Distribution . . . . . 108

7. CONCLUSIONS . . . . . 112

7.1 Summary . . . . . 112

7.2 Future Work . . . . . 113

REFERENCES . . . . . 115

APPENDIX A - GENERALIZED OHM'S LAW . . . . . 119

APPENDIX B - RADIAL MASS CURRENTS IN THE ARC . . . . 122

APPENDIX C - INTENSITY RATIO OF THE LINES He II 4686 Å AND He I 4471Å . . . . . 125

# LIST OF FIGURES


| Figure | | Page |
|---|---|---|
| 1.1 | Electron-ion collision times in helium versus temperature . . . . . | 9 |
| 1.2 | Magnetic field $\vec{B}$, current density $\vec{j}$, azimuthal velocity $\vec{v}_\phi$, and the two coordinate systems . . . . . | 12 |
| 1.3 | Mass currents in the arc (scheme) . . . . . | 18 |
| 2.1 | Component $B_z$ of the magnetic field versus z and radius . . . . . | 28 |
| 2.2 | Magnetic field and arc apparatus . . . . . | 29 |
| 2.3 | Timing of the plasma with respect to the magnetic field . . . . . | 34 |
| 3.1 | Halfwidth of the line He I 4471 Å versus electron density . . . . . | 43 |
| 3.2 | Ratio of intensities of two helium lines versus temperature . . . . . | 44 |
| 3.3 | Theoretical static ionization relaxation time of doubly charged helium ions versus temperature . . . . . | 51 |
| 3.4 | Optical system for time resolved spectroscopy and photography . . . . . | 54 |
| 4.1 | Laser interferometer . . . . . | 66 |
| 4.2 | Laser interferograms . . . . . | 69 |
| 5.1 | Shape of the electron and ion components as a function of parameter $\alpha$ for case $T_i=T_e$ . . . . . | 77 |
| 5.2 | Apparatus for the laser scattering experiment . . . . . | 81 |

| Figure | | Page |
|---|---|---|
| 5.3 | Details of Figure 5.2 (a) Spark gap for triggering the Pockels cell (b) Pulsed ruby laser . . . . . | 82 |
| 5.4 | Block diagram of the triggering components and timing for laser scattering . . . . | 84 |
| 5.5 | Oscillogram of the scattered and reference pulses . . . . . | 85 |
| 6.1 | Smear pictures of the arc at varying values of the filling pressure, plasma current, and magnetic field . . . . . | 88-90 |
| 6.2 | Frequency of arc rotation versus magnetic field . . . . . | 93 |
| 6.3 | Laser scattering profile . . . . . | 96 |
| 6.4 | Radial electron density distribution in the arc . . . . . | 97 |
| 6.5 | Radial electron density distribution in the arc . . . . . | 98 |
| 6.6 | Radial temperature distribution in the arc . . . . . | 100 |
| 6.7 | Radial distribution of total and partial pressures in the arc . . . . . | 111 |
| 6.1A | Unstationary arc in magnetic field (colour) . . . . . | 91 |

# LIST OF TABLES

Table Page

1 Comparison of the Most Important Parameters of the Apparatus Reported in this Thesis and in References [1-7] . . . . . 114

# ACKNOWLEDGEMENTS

I wish to thank Dr. J. Meyer for suggesting and supervising this work. He was always prepared to discuss the experimental and theoretical aspects of the work. The scattering experiment was done in cooperation with him.

G.G. Albach has built a five channel detector for future laser scattering experiments from the arc, described in this thesis. He also read the manuscript of the thesis.

J.M. Preston and D.C. Stevenson contributed their knowledge of laser interferometry.

Dr. A.J. Barnard folded the theoretical line profile of He I 4471 Å with the instrumental profile.

The Plasma Physics Group is a fine working collective, which made my stay in Canada pleasant.

Special thanks go also to the technical staff, particularly to D. Sieberg, D. Haines and J. Lees.

This work is supported by a grant from the Atomic Energy Control Board of Canada.

# INTRODUCTION

For laser scattering and many other investigations it is desirable to produce a magnetized high temperature high density plasma in a steady state. Two plasma sources come to mind immediately: (1) a wall stabilized arc and (2) a magnetically stabilized arc.

In a cylindrically symmetrical wall stabilized arc in a steady state the properties of the plasma in the arc column are mainly determined by the radial conductive energy loss according to the equation of conservation of energy [6]. This energy loss is replaced by Ohmic heating. Because the thermal conductivity is a strong function of temperature, the conductive energy loss increases with the arc's axial temperature. The power supplied per unit length of the arc column therefore also increases strongly with the desired increase of the arc's axial temperature. A wall stabilized arc is therefore not very suitable for producing high temperature plasmas.

A magnetically stabilized helium arc of the type described by Wulff [1] is a better source of a high temperature plasma because in a magnetic field the thermal conductivity can be drastically reduced in the plane perpendicular

to the magnetic field. A longitudinal magnetic field decreases the radial conductive energy loss. Consequently, for high magnetic fields, higher temperatures should be possible in a magnetically stabilized arc than in a wall stabilized arc. However, the experiments conducted on magnetically stabilized arcs [1-5] showed that the highest temperature obtainable in such arcs is limited by dynamic phenomena. To understand this phenomenon the equation of motion and the generalized Ohm's law should be considered beside the energy conservation equation.

In the arc designed by Wulff, axial arc temperatures exceeding 200,000 °K were obtained [1-5]. These temperatures were estimated from the spectroscopic data. The spectroscopic determination of plasma temperature of that magnitude is complicated, inaccurate and sometimes even questionable [7]. A laser scattering experiment yielded a surprisingly low axial temperature of 40,000 °K [8] most likely because the arc apparatus was not properly designed for laser scattering experiments.

With laser scattering as one of the main diagnostic techniques in mind, we have built a similar magnetically confined arc. Construction principles and diagnosis of this arc using several conventional methods are described in this thesis, so that with the present results at hand, the laser scattering from the arc plasma can be studied. Since the light scattering experiments require viewing ports

in a plane perpendicular to the magnetic field line and only a small capacitor bank was available, a change in the design of the Wulff's "hourglass" [1] was necessary.

As the plasma parameters depend on the geometry of the apparatus, the experimental data reported in [1-5] were not relied upon without verification. This report therefore contains an extensive study of radial distribution of plasma parameters using a variety of techniques: time resolved photography and spectroscopy, laser interferometry, and laser scattering. Particular attention was given to the measurement of the electron temperature and density in the hot core of the arc. Due to unreliability of spectroscopic measurements at high temperatures, laser interferometry was used to measure the radial electron density distribution in the hot core of the arc. Laser scattering was added for two reasons: Firstly to show that the design is good for future laser scattering experiments and secondly, to measure the axial electron temperature and axial electron density. Laser interferometry and laser scattering were used successfully for the first time to measure the plasma parameters of a magnetically stabilized arc.

It turns out that the geometry of the apparatus is very important for a magnetically stabilized arc, therefore Chapter 1 contains an outline of the theory of an arc in a longitudinal magnetic field. Ideas obtained

in this chapter lead to the construction of the apparatus given in Chapter 2. Properties of the arc are studied and the measurements are described in Chapters 3, 4, and 5. The results of these investigations are presented in Chapter 6. Chapter 7 summarizes the important aspects of this work,which is meant to be the starting point for laser scattering experiments in a fully ionized, magnetized plasma.

# Chapter 1

# THEORY OF ELECTRIC ARC IN A LONGITUDINAL MAGNETIC FIELD

The highest temperatures that can be reached in a stationary arc are controlled by the energy loss mechanisms. The simplest example is a cylindrically symmetric arc in which the energy loss is mainly due to the heat conduction according to the equation

$$\frac{1}{r}\frac{\partial}{\partial r}\left(r\,\kappa\,\frac{\partial T}{\partial r}\right) + j_z\,E_z = 0 \qquad (1.1)$$

where $\kappa$ is the thermal conductivity of the plasma. The relationship between the axial electric field $E_z$ and axial current density $j_z$ is given by Ohm's law.

$$j_z = \sigma E_z \qquad (1.2)$$

In the column of a cylindrically symmetric, wall stabilized arc the electric field $E_z$ is constant over the arc length and cross section,

therefore the radial distribution of the electric current density is determined by the radial distribution of electrical conductivity.

The solution of eqs. (1.1) and (1.2) shows that the temperature of such an arc depends only on the energy dissipated per unit length of the arc, $E_z I$, where I is the arc current. Because the heat conductivity increases strongly with temperature ($\kappa \propto T^{5/2}$) the axial arc temperature increases slowly with the energy input.

In order to increase the axial temperature one can decrease the thermal conductivity by putting the arc into an externally applied magnetic field. The magnetic field reduces the thermal conductivity in the plane perpendicular to the magnetic field lines. The arc behaviour is affected strongly only when the electron cyclotron frequency is greater than the electron-ion collision frequency.

The axial temperatures obtained experimentally in arcs in a magnetic field however were much lower than those predicted by the energy conservation equation (1.1) for a given energy input. The reason for this is that the dynamics of the arc plasma which is not described by the energy conservation equation becomes important in the presence of a magnetic field.

The magnetic field induces azimuthal electric currents that cause a strong pressure increase at the arc

axis. The resulting higher pressure reduces the effect of the magnetic field on the axial temperature since the collision frequency is increased at the same time. These phenomena will be discussed in section 1.1 of this chapter.

The magnetic field influences the current density and electric field distributions. An important mechanism for the distribution of these two parameters is the rotation of the arc. Section 1.2 of this chapter is devoted to these problems.

The magnetic field also induces axial and radial mass currents. The radial currents are responsible for the shift of ionization equilibrium (see Chapter 3, 3.1, 3.2). The radial mass currents will be dealt with in Appendix B.

## 1.1 Pressure Increase

A helium plasma consists in general of four components: electrons, once and twice charged ions and neutrals. Because of the high ionization energy of helium ($\simeq$ 24 eV for the first ionization, $\simeq$ 54 eV for the second ionization) the arc can be divided into the following zones:

1. Close to the arc axis one observes a two component plasma consisting of electron and doubly charged helium ions provided that the temperature is high enough.

2. In a region at larger radii there exists a three component plasma containing electrons, once charged ions and doubly charged ions.
3. The next zone is again a two component region with electrons and once charged ions.
4. At the arc boundary one observes three components: electrons, once charged ions and neutral atoms.

This division of the arc considerably simplifies the equations used in the study of the arc dynamics discussed in the following sections.

A very important parameter of a magnetized plasma is the product of electron cyclotron frequency $\omega_e (\omega_e = \frac{eB}{m})$ and electron-ion collision time $\tau_e$. The magnetic field affects the plasma parameters strongly when $\omega_e \tau_e >> 1$. In all calculations of this thesis it is assumed that the inequality $\omega_e \tau_e >> 1$ is satisfied.

In a helium plasma in regions where neutral atoms are absent the electron-ion collision time is a combination of electron collision time with once and twice charged ions [9, p. 259].

$$\frac{1}{\tau_e} = \frac{1}{\tau_{e1}} + \frac{1}{\tau_{e2}} \qquad (1.3)$$

where:

$$\tau_{eZ} = \frac{3\sqrt{m_e}\left[KT_e\right]^{3/2}\left[4\pi\varepsilon_0\right]^2}{4\sqrt{2\pi}\ Z^2e^4\ n_Z\ \ell n\ \Lambda} \tag{1.4}$$

where Z is equal to 1 or 2.

In eq. (1.4) $\ell n\ \Lambda$ is the Coulomb logarithm, $n_Z$ is the ion density. The other symbols have their usual meaning.

In Fig. 1.1 the electron ion collision time is plotted as a function of temperature. In the calculation of $\tau_e$ the ion densities $n_2$ and $n_1$ are expressed in terms of the electron density as measured in this experiment (Fig. 6.4) and in terms of the ratio of densities of twice to once charged helium ions $n_2/n_1$ as measured by Bergstedt [5] and discussed in Chapter 3 of this report. It can be seen that at all temperatures $\omega_e\tau_e >> 1$ for B = 4.0 T.

In order to explain the pressure increase in the arc two equations have to be discussed: the equation of motion (1.5) and generalized Ohm's law (1.6); the latter equation is derived in Appendix A.

$$\rho\ \frac{d\vec{v}}{dt} + D(n\vec{v}) + \nabla p + \vec{R}_{ei} = \vec{j} \times \vec{B} \tag{1.5}$$

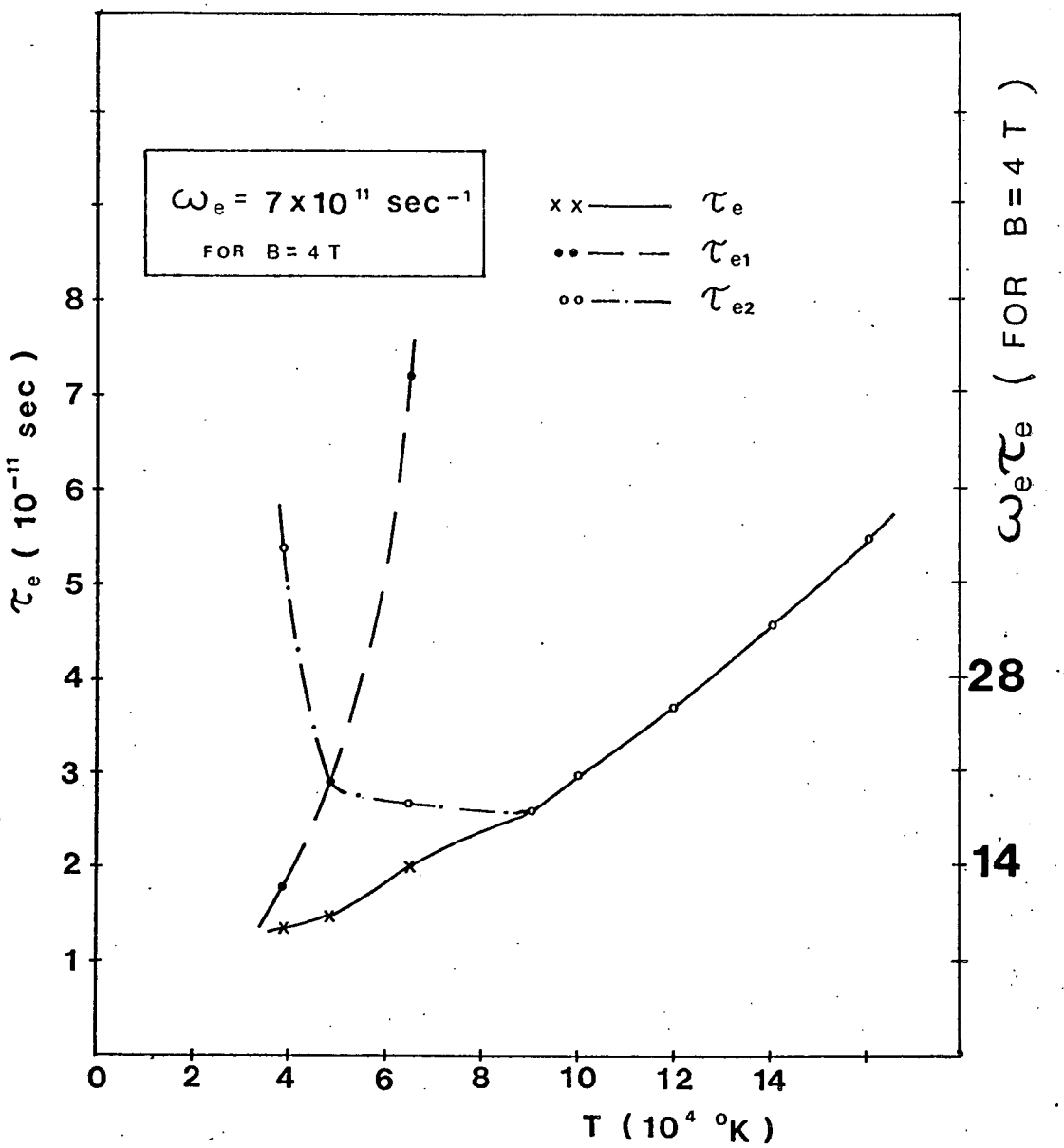


Figure 1.1 Electron-ion collision times in helium versus temperature.

$$\frac{1}{\sigma_{\parallel}}\vec{j}_{\parallel} + \frac{1}{\sigma_{\perp}}\vec{j}_{\perp} = \vec{E} + (\vec{v} + \vec{d}) \times \vec{B} - \frac{1}{en_e}\vec{j} \times \vec{B} + \frac{1}{en_e}\nabla p_e$$

$$+ \frac{K}{e}\left(\gamma_{\perp}\nabla_{\perp}T + \gamma_{\parallel}\nabla_{\parallel}T\right) - \frac{3}{2}\frac{K}{e\,\omega_e\tau_e}\nabla T \times \frac{\vec{B}}{B} \qquad (1.6)$$

Equation (1.5) is written in the centre of mass system. $\vec{v}$ is centre of mass velocity. $\vec{R}_{ei}$ is the force of internal friction. Symbols $\perp$ and $\parallel$ relate to the co-ordinate system introduced below. $\partial\vec{j}/\partial t = 0$ was assumed.

$$\vec{d} = \begin{cases} \dfrac{n_0}{n_1 + n_0}\vec{d}^{(10)} & \text{for } n_2 = 0 \\ \\ \dfrac{n_1 n_2}{n_e(n_1 + n_2)}\vec{d}^{(21)} & \text{for } n_0 = 0 \\ \\ 0 & \text{for a two component plasma} \end{cases}$$

where $\vec{d}^{(iK)} = \vec{v}_i - \vec{v}_K$ is the relative velocity of heavy particles with respect to one another ($\vec{v}_2$, $\vec{v}_1$, $\vec{v}_0$ are the velocities of twice ionized, once ionized and neutral helium particles).

$D(\eta\vec{v})$ is a differential expression involving the spatial derivatives of the second order; $\eta$ is the arc viscosity. Other symbols have their usual meaning.

The force of internal friction $\vec{R}_{ei}$ is discussed in more detail in Appendix A, where the generalized Ohm's law is derived.

Due to the curvature of the magnetic field lines it is convenient to split the magnetic field into a meridional component $\vec{B}_m$ (in r-z plane) and an azimuthal component $B_\phi\vec{e}_\phi$. $\vec{B} = \vec{B}_m + B_\phi\vec{e}_\phi$. It is also convenient to use a coordinate system defined with unit vectors $\vec{e}_\phi$, $\vec{e}_{\parallel} = \vec{B}_m/B$ and $\vec{e}_\perp = \vec{e}_\phi \times \vec{e}_{\parallel}$. Then it is by def. $B_\perp = 0$.

The electric current density $\vec{j}$ will also be split into a meridional component $\vec{j}_m$ and an azimuthal component $\vec{j}_\phi$ as will be $\vec{v}$ and $\vec{d}$. The relationship between vectors $\vec{j}$ and $\vec{B}$, cylindrical and $(\vec{e}_\perp, \vec{e}_\phi, \vec{e}_{\parallel})$ coordinate systems are shown in Figure 1.2. At the center of the discharge (at $z = 0$) the two coordinate systems are approximately equivalent.

For the discussion of axial pressure increase the friction force will be neglected and a steady state will be assumed. The $\perp$ component of eq. (1.5) is then

$$\nabla_\perp p = \vec{j}_\phi \times \vec{B}_m + \vec{j}_{m\parallel} \times \vec{B}_\phi = (j_\phi B_m - j_{m\parallel} B_\phi)\vec{e}_\perp \qquad (1.7)$$

The first term on the right hand side of this equation gives the pressure increase due to induced azimuthal currents. The second term is the pressure increase due to the classical pinch effect.

The azimuthal current density $\vec{j}_\phi$ is given by the $\phi$ component of eq. (1-6):

$$j_\phi \vec{e}_\phi = \sigma_\perp (\vec{v}_{m\perp} - \frac{1}{en_e} \vec{j}_{m\perp} + \vec{d}_{m\perp}) \times B_m - \frac{1}{B_m^2} \frac{3}{2} n_e K \nabla_{m\perp} T \times \vec{B}_m$$

$$+ (1 - \frac{\sigma_\perp}{\sigma_\parallel}) \frac{\vec{j}_m \vec{B}_m}{B^2} B_\phi \vec{e}_\phi \quad . \qquad (1.8)$$

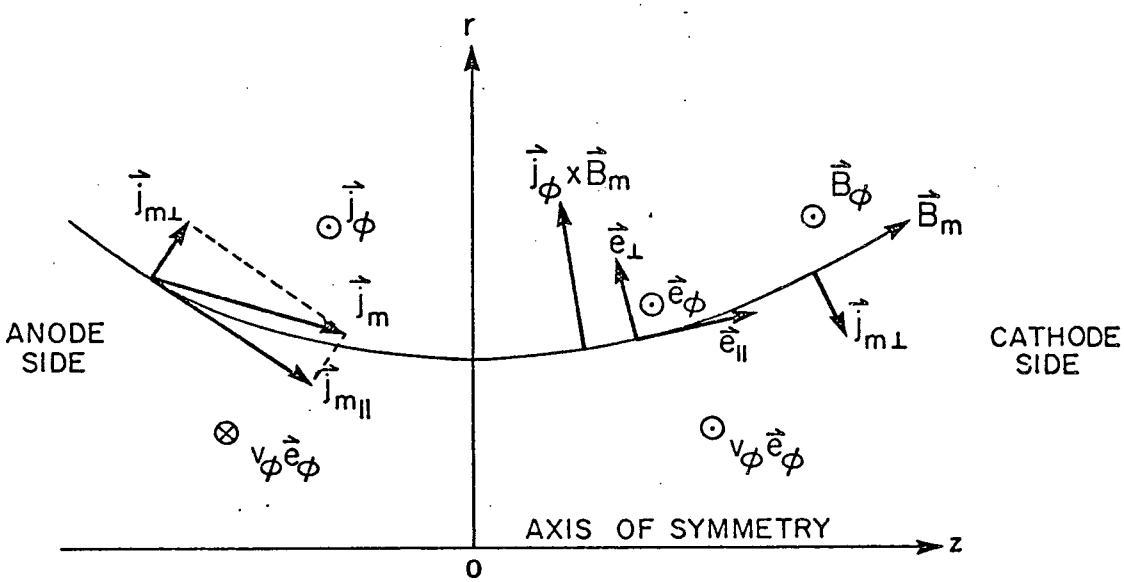


Figure 1.2 Magnetic field $\vec{B}$, current density $\vec{j}$, azimuthal velocity $\vec{v}_\phi$, and the two coordinate systems.

$\vec{j}_{m\perp} = \frac{1}{B_m^2}[\vec{B}_m \times (\vec{j}_m \times \vec{B}_m)]$ is the perpendicular part of the meridional component of electric current density (see Figure 1.2). Vectors $\vec{v}_{m\perp}$ and $\vec{d}_{m\perp}$ are defined in a similar way.

Now the significance of the terms in equation (1.8) and the importance of their contribution to the pressure gradient can be discussed.

The terms of eq. (1.8) describe the following effects: The first term ($\propto \vec{v}_{m\perp} \times \vec{B}_m$) causes a pressure gradient due to mass currents.

The second term ($\propto \vec{j}_{m\perp} \times \vec{B}$) is due to Hall effect. The third term ($\propto \vec{d}_{m\perp} \times \vec{B}_m$) is the azimuthal current density caused by the ambipolar diffusion of electrons and ions. The fourth term ($\propto \nabla_{mT} \times \vec{B}$) describes the thermomagnetic or Nernst effect. The fifth term describes the pinch effect that arises due to anisotropy of the electrical conductivity.

### 1.1.1 Thermomagnetic or Nernst Effect

When a temperature gradient perpendicular to the magnetic field is present a voltage is induced (due to electron-ion collisions) perpendicularly to $\vec{B}$ and grad T. This is the so called Nernst effect calculated for a plasma by Braginskii [10] and first observed in an arc by Kluber [2] In our case it is directed azimuthally and causes a pressure increase in the discharge. It is a dominant cause of

the pressure increase at the arc axis in the middle of the discharge configuration.

At z = 0 the cylindrical coordinate system can be used as an approximation. The pressure gradient arising from the Nernst effect alone is then:

$$\frac{\partial p}{\partial r} = \frac{3}{2} n_e K \frac{\partial T}{\partial r} \tag{1.9}$$

Combining this equation with the equation of state for a quasineutral plasma with the ions of charge Z

$$p = \frac{Z + 1}{Z} n_e KT \tag{1.10}$$

the following equation is obtained:

$$\frac{Z + 1}{Z} n_e K \frac{\partial T}{\partial r} + \frac{Z + 1}{Z} KT \frac{\partial n_e}{\partial r} = \frac{3}{2} n_e K \frac{\partial T}{\partial r} \tag{1.11}$$

For a doubly ionized helium plasma Z = 2 and

$$\frac{\partial n_e}{\partial r} = 0 \quad \text{or} \quad n_e = \text{const.}$$

This result was proven experimentally (see Chapter 6).

### 1.1.2 Ambipolar Diffusion

This effect in an arc was first studied by Wienecke [11]. In the outer zones of the arc, where the three component plasma is found, the pressure is increased due to diffusion of charged particles and neutrals. The diffusion is important at the boundary between regions of neutral atoms and once charged ions as well as at the boundary between regions of once and twice ionized helium.

At the former boundary electrons and ions diffuse outwards (due to their partial pressure gradients) and the neutrals inwards. The diffusion of the ions is hindered by the magnetic field and therefore a net flow of particles is directed inwards and the pressure increases in the direction of increasing degree of ionization. In a stationary state an aziumthal current flows, equal to

$$j_{\phi A} = \sigma_{\perp} \frac{n_0}{n_1 + n_0} (v_1 - v_0)_r B_z$$

According to eq. (1.7) the electromagnetic force balances the pressure gradient.

Similar considerations are true for the boundary between once and twice ionized helium. The total pressure increase due to ambipolar diffusion is proportional to $B_z$.

### 1.1.3 Pinch Effect

For easier understanding of the following sections the reader is first referred to the Figure 2.2, Chapter 2 which shows the plasma apparatus. Note the geometry of the discharge tube, particularly the presence of glass funnels, whose surfaces coincide with a magnetic flux tube. The narrow throat of the funnels plays an important role in the dynamics of the arc as it will become clear from the discussion below.

The pressure increase due to the pinch effect is represented by two terms: the second term of eq. (1.7) and the last term of eq. (1.8). For high magnetic fields ($\omega_e\tau_e >> 1$) one observes $\sigma_\parallel \simeq \frac{1}{2}\sigma_\perp$ [10]. It can be easily seen that the anisotropy of the electric conductivity reduces the pressure increase due to the classical pinch effect by approximately a factor of 2. The pinch effect is unimportant in the middle of the discharge, but becomes important (compared to other effects) at the glass funnels.

### 1.1.4 Hall Effect

The term $\vec{j}_\phi^{(H)} = -\frac{1}{en_e}\vec{j}_{m\perp} \times \vec{B}_m$ can increase or decrease the pressure, depending on the sign of $\vec{j}_{m\perp}$. In sec. 1.2 it is shown that in a real plasma the electric current does not flow parallelly to the magnetic field lines. $j_{m\perp}$ cuts the field lines outwards at the anode funnel and inwards at the cathode funnel. The Hall effect

therefore increases the pressure in the cathode region and decreases it in the anode region. It is important only at the ends of glass funnels.

### 1.1.5 Mass Currents in the Arc

Mass currents influence the pressure distribution too. The influence is described by the term $\vec{j}_\phi = \sigma_\perp \vec{v}_m \times \vec{B}_m$ of eq. (1.8). The radially inward flowing particles decrease the pressure, the outward flowing particles increase the pressure. The mass currents are present in the arc for the following reason: The pressure at the center of the arc configuration (where the magnetic field is high) is higher than near the glass funnels (where the magnetic field is low). Consequently, at the arc axis the plasma streams from the center of the system towards the funnels. If the arc is stationary, the axial outflow has to be replaced by radial inflow of the particles. The flow pattern is schematically shown in Figure 1.3. The magnitude of this contribution to the pressure is difficult to evaluate. The radial mass velocity (at $z = 0$) will be calculated in Appendix B.

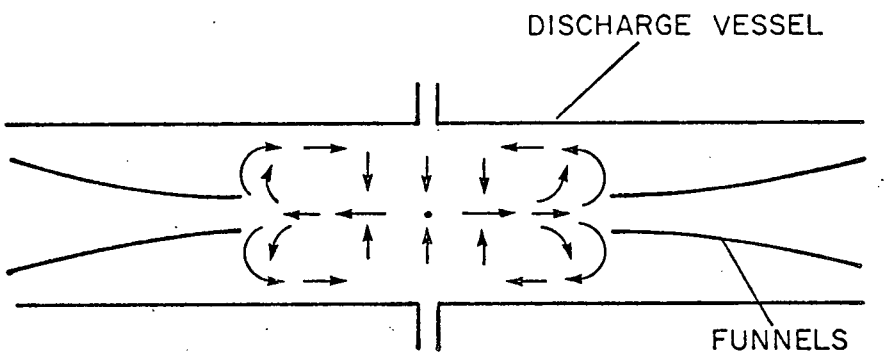


Figure 1.3 Mass currents in the arc (scheme).

In this section it was shown that the Nernst effect, ambipolar diffusion and pinch effect are diamagnetic in nature (the anisotropy of electric conductivity gives a paramagnetic contribution to the pinch pressure). The Hall effect and mass currents can be either paramagnetic or diamagnetic, depending on the geometry of the discharge.

In the following section the effect of the magnetic field on electric current and field distribution will be discussed.

## 1.2 Distribution of the Electric Current, Electric Field and Arc Rotation

The equation of motion (1.5) and the generalized Ohm's law (1.6) in the coordinate system ($\vec{e}_\perp$, $\vec{e}_\phi$, $\vec{e}_\parallel$) may as well be used for the discussion of the electric current and field distribution. As only the components of the electric current density and velocity with respect to the meridional magnetic field will be used the notation will be simplified by writing $\vec{j}_{m\perp} \equiv \vec{j}_\perp$, $\vec{j}_{m\parallel} \equiv \vec{j}_\parallel$, $v_{m\perp} \equiv \vec{v}_\perp$ etc. According to equations (1.5) and (1.6) the arc rotation is closely linked to the electric current distribution in the arc.

At the beginning of the discharge the arc column spreads radially outwards. Therefore an electric current flows perpendicular to the magnetic field $\vec{B}_m$. At the anode an electric current density $j_\perp > 0$, and correspondingly at the cathode a component $j_\perp < 0$ are set up. The spread of the arc is hindered by electromagnetic forces. According to eq. (1.5) the azimuthal force density $(-j_\perp B_m \vec{e}_\phi)$ sets the arc into rotation in the opposite sense in front of each electrode. The direction of rotation is such that the induced electric field $v_\phi B_m \vec{e}_\perp$, obtained from eq. (1.6) and from Lenz's rule, points in the direction opposite to $j_\perp \vec{e}_\perp$. Moreover, according to eq. (1.6) one may write:

$$j_\phi = \frac{\sigma_\perp}{en_e} j_\perp B_m - \sigma_\perp v_\perp B_m = j_\phi^{(H)} - \sigma_\perp v_\perp B_m. \quad (1.13)$$

The Hall component of the electric current density $j_\phi^{(H)}$ as expressed by the Hall term of eq. (1.13) leads to an induced voltage $(-\sigma_\perp B_m^2 \, j_\perp \vec{e}_\perp / e^2 n_e^2)$ which also counteracts the current $j_\perp \vec{e}_\perp$.

The energy dissipated in the arc due to the presence of $j_\perp$ is given by $(j_\perp B_m v_\phi)$. In a frictionless arc this energy is used to increase the rotational velocity. This velocity increases as long as $j_\perp \neq 0$. A stationary state is reached when $v_\phi$ has increased to such a value that the induced voltage $v_\phi B_m \vec{e}_\perp$ reduces the perpendicular current density to zero. With the vanishing of $j_\perp$ also the Hall azimuthal current density disappears.

In a frictionless plasma in a stationary state one may set: $j_\perp = 0$. The current density distribution setup is such that $j_m$ is parallel to $\vec{B}_m$, since a non-vanishing force $\vec{j}_m \times \vec{B}_m$ is incompatible with a stationary equilibrium. Equation (1.6) in component form is:

$$\frac{1}{\sigma_\parallel} j_\parallel = E_\parallel + v_\perp B_\phi + \frac{1}{e n_e} \nabla_\parallel p_e \qquad (1.14)$$

$$0 = E_\perp + v_\phi B_m - v_\parallel B_\phi + \frac{1}{e n_e} \nabla_\perp p_e \qquad (1.15)$$

Because no current flows across the magnetic flux tube distinguished by the electrodes, $j_\parallel$ must varnish outside that flux tube. There $E_\parallel$ must compensate the electric

fields $v_\perp B_\phi$ and $\nabla_\parallel p/en_e$. Inside the flux tube one may set $E_\parallel \simeq j_\parallel/\sigma_\parallel$. The electric field $E_\parallel$ outside the flux tube in most cases is small compared to $E_\parallel$ inside the flux tube.

According to eq. (1.15) one can write $E_\perp \simeq -v_\phi B_m$. The other terms are much smaller. This electric field balances the current density across the magnetic field. In this experiment $E_\perp$ is of the order of magnitude of a few hundred V/cm.

In a plasma with finite internal friction stationary states with $j_\perp \neq 0$ are possible. The work of $j_\perp$ done on a plasma ($- \int j_\perp B_m v_\phi \, dV$) can be converted into heat by the internal friction. This work therefore does not necessarily lead to an increase in rotational energy of the arc. A stationary electric current distribution with $j_\perp \neq 0$ is then naturally determined also by the Hall current. Which of the two processes is more important: the arc rotation or the Hall effect depends on the arc geometry, on the parameter $\omega_e \tau_e$ - the product of electron gyrofrequency and electron-ion collision time, as well as on the plasma viscosity.

## 1.3 Unstationary States of the Arc

A quantitative theoretical analysis of the unstationary state of the arc is too involved to be given in the scope of this thesis. It would mean that the time and

spatially dependent combination of the equation of motion (1.6) and generalized Ohm's law (1.7) should be solved. The boundary conditions are extremely complex because of the asymmetric funnel configuration.

Only a qualitative description of processes that cause the unstationary behavior of the arc will be given here. In section 1.1.5 it was shown that due to the magnetic field the pressure is increased at the arc axis and axial mass currents flow from the midplane between the electrodes ($z = 0$) towards the glass funnels, where the magnetic field and consequently the pressure are smaller. In a stationary state the axial mass outflow has to be replaced by radial inflow. When the radial mass inflow is prevented the arc becomes unstationary.

For an illustration of this problem the simplest form of equation of motion (1.5) and Ohm's law (1.6) will be used.

$$\rho \frac{d\vec{v}}{dt} \equiv \rho \left[\frac{\partial \vec{v}}{\partial t} + \nabla\left(\frac{v^2}{2}\right) - \vec{v} \times (\nabla \times \vec{v})\right] = -\nabla p + \vec{j} \times \vec{B} \tag{1.16}$$

$$\vec{j} = \sigma(\vec{E} + \vec{v} \times \vec{B}) \tag{1.17}$$

If these two equations are combined in component form and if it is assumed that the motion is stationary and rotationally symmetric, the radial velocity of the

ionized matter is obtained in the form

$$v_r = \frac{B_r}{B_z} v_z - \frac{1}{\sigma B_z^2} (j_z B_\phi + \nabla_r p + T_r) \qquad (1.18)$$

$T_r$ is the radial component of the inertial part of the equation of motion. It was transferred to the right hand side because it contains derivatives of $v_r$ which are small compared with $v_r$ itself.

$$T_r = \rho(v_r \frac{\partial v_r}{\partial r} - v_z \frac{\partial v_r}{\partial z} - \frac{v_\phi^2}{r})$$

In the equation (1.18) only the term $- \frac{1}{\sigma B_z^2} j_z B_z$ represents the radial inflow. If the magnetic field or the conductivity are increased above a critical value the mass inflow will become small and the arc will be unstationary. As the conductivity $\sigma$ varies $\propto T^{3/2}$, the unsteady state can be reached by increasing the arc temperature which can be achieved e.g. by increasing the arc current.

If one however succeeds in making the outflow terms (e.g. 1.18) small at the same time, one may maintain the arc in a steady state. Of the outflow terms $(\frac{B_r}{B_z} v_z)$ is the most important one, because it includes the curvature of the magnetic field lines expressed in the $B_r$ component. Since the plasma flows axially away from the center and the field lines are convex with respect to the arc axis

this term is always positive representing a radial outflow. The magnetic field lines of a short coil diverge faster than those of a long coil, therefore, the radial inflow should be prevented more strongly in a magnetic field of a short coil.

In conclusion of this chapter it may now be predicted that in a magnetized helium arc the following effects will be observed: high axial temperature and pressure, approximately constant electron density around the arc axis as well as stationary and unstationary arc rotation.

# CHAPTER 2

# DESIGN OF THE APPARATUS

The task of building a magnetically stabilized arc can be divided into two parts: production of the magnetic field and production of the plasma. The former is described in section 2.1 the latter in section 2.2.

## 2.1 Production of High Magnetic Field

The theory of an electric arc in a longitudinal magnetic field outlined in Chapter 1, calls for a magnetic field higher than about 3.0 Teslas. However, the higher the magnetic field the more it will influence the plasma properties. The ultimate choice of the magnitude of the magnetic induction depends on the available energy, the volume in which the magnetic field has to be high and the duration of the field.

A pulsed magnetic field is an obvious choice, because a continuous field in a volume desired for this experiment ($\simeq$ 50 $cm^3$) requires about one MW of power. Yet the magnetic field pulse has to be long enough to be con-

sidered continuous in comparison with the length of the plasma pulse.

The magnetic field must be symmetrical to a high degree, because the arc symmetry is very dependent on the symmetry of the magnetic field. The field homogeneity is also important.

Two identical Bitter-type coils*[12] were built. They were mounted together in a Helmholtz configuration, providing a 2 cm wide gap at the center. The gap was necessary for the observation of the plasma and for an easy access to the arc in the laser scattering experiment.

Each coil was built in the following way: A copper bus bar (1.6 cm wide, 0.3 cm thick) was bent into a helix of 32 turns. The turns were isolated from each other with mylar. The coil was cast in epoxy which provided the necessary mechanical rigidity. (At a magnetic field of 5.0 Teslas the maximum radial tensile stress is about 150 atm; the axial force between the two coils is over $2 \times 10^5$ Newtons).

The electrical circuit is shown in Figure 2.2. A 29 kJ capacitor bank (5 kV, 2.2 mF) was discharged through the coil to produce a damped oscillation. Two ignitrons (rated at 15 kV, 35 kA) were the switching elements. The data of the apparatus are summarized below:

---

*The radial electric current density distribution of a Bitter coil is inversely proportional to radius.

| | | |
|---|---|---|
| Each Coil: | Inside diameter | : 7.0 cm |
| | Length | : 13 cm |
| | Inductance | : 35 μH |
| Circuit: | Capacitance | : 2.2 mF |
| | Energy | : 29 kJ |
| Period of Oscillation: | 2.65 msec. | |

Due to the low damping constant of the electrical circuit 78% of the capacitor energy was stored in the magnetic field at the first magnetic field maximum.

The spatial distribution of the magnetic field was measured with a magnetic pickup coil [13]. Figure 2.1 shows the measured z component of the magnetic field $B_z$ (z-axis coincides with the axis of the coils) vs. z at two radial positions.

From the magnetic field distribution the magnetic field lines (flux tubes) were constructed. The field lines are plotted in Figure 2.2.

No asymmetry of the magnetic field was detected within the error of measurement of less than 5%.

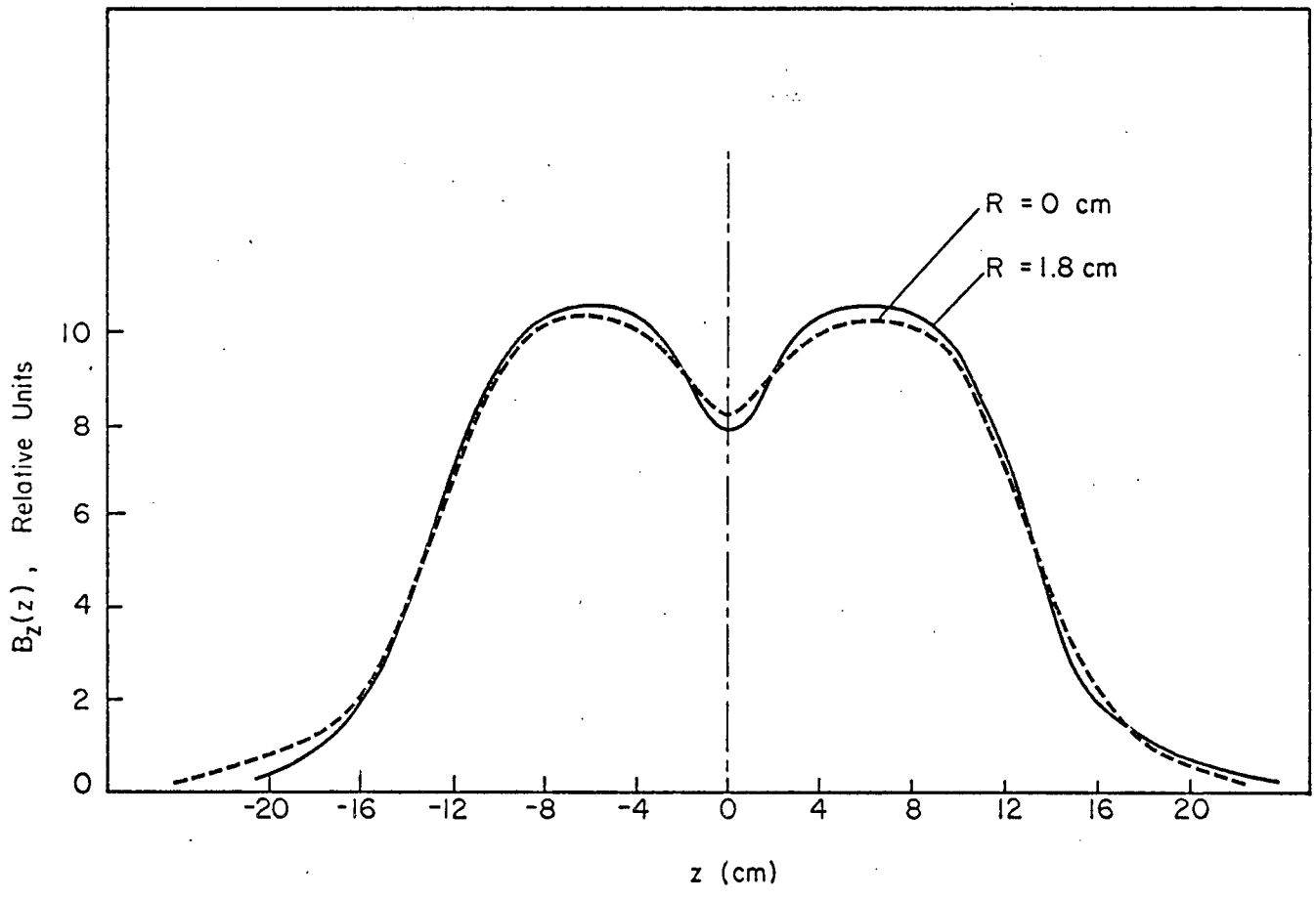


Figure 2.1 Component $B_z$ of the magnetic field versus z and radius.

Figure 2.2 Magnetic field and arc apparatus.

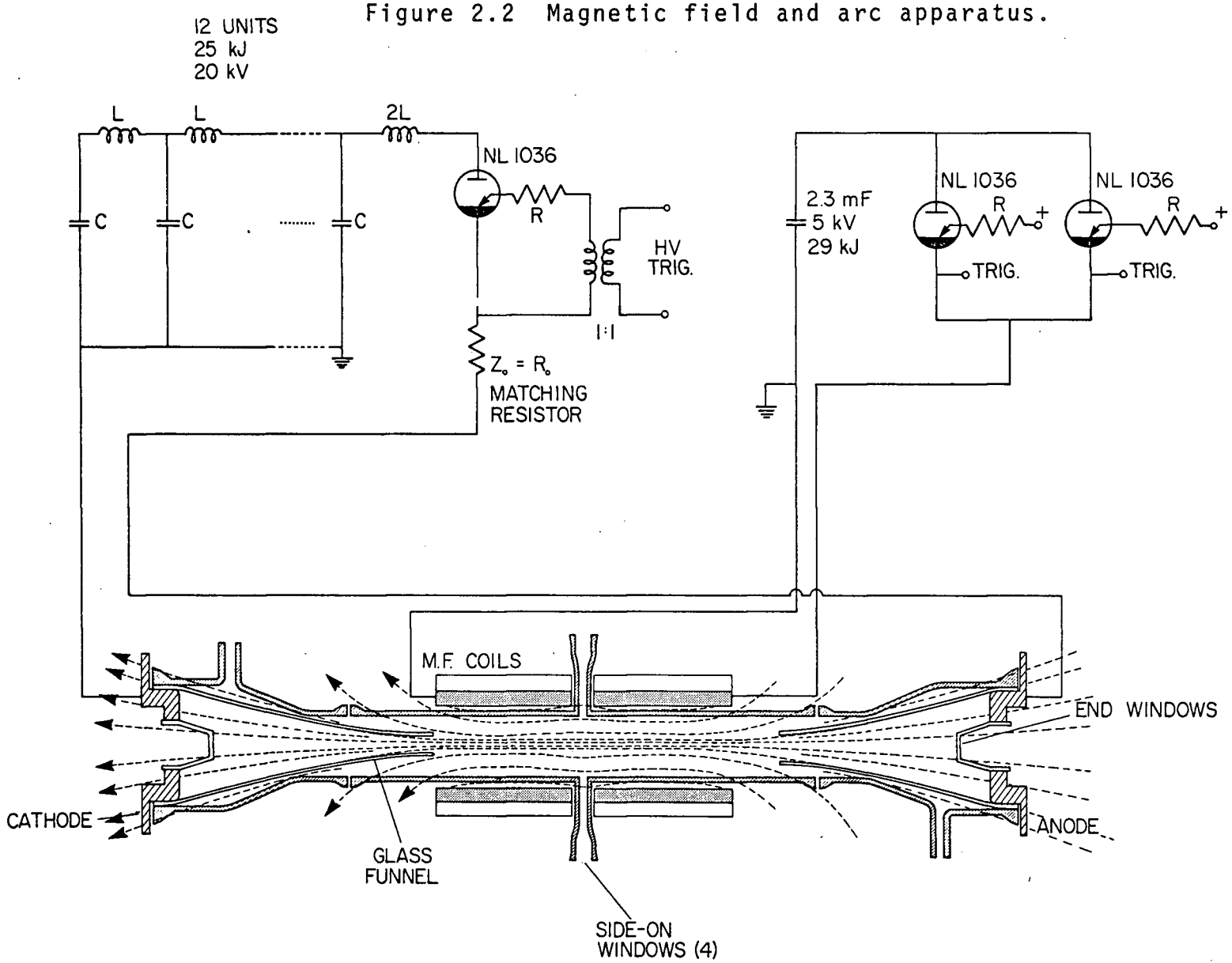

## 2.2 Discharge Design

### 2.2.1 Discharge Tube

In the introduction it was mentioned that the arc was built for the study of laser light scattering from plasmas in a high magnetic field. The following design criteria were determined by this goal:

(a) A steady, stable and reproducible arc to give small errors in shot to shot measurements.

(b) High temperature to ensure full ionization and low collision frequencies.

(c) High electron density to give a large scattering signal.

(d) The scattering plane perpendicular to the magnetic field.

(e) Large enough ports should be built to allow the entrance and exit of the laser beam without illuminating the glass tube and to ensure a reasonably large solid angle of the scattering observation optics.

These requirements are interconnected. A high temperature arc cannot be built if it is not reasonably steady and stable.

The requirement (e) contradicts the first three. Large observation windows mean that the magnetic field

coils have to be separated by a large distance. This makes the magnetic field inhomogeneous in the arc region. The magnetic field inhomogeneity is partly responsible for the unsteady behaviour of the arc, in particular the presence of $B_r$ component (see Chapter 3).

In the design of the discharge a compromise among the above criteria had to be made. The theoretical calculations of dynamical behaviour of the arc, discussed in Chapter 1, were also born in mind. However, no quantitative calculations could be done. The theory was only a qualitative guide to proper design.

Similar "hourglass" shaped discharges have been built before [1-5]. The experimental findings on those discharges were also considered.

The important factors in the discharge design for a given magnetic field distribution are summarized in the following:

1. The electrodes should be far apart and as wide as possible. Narrow electrodes carry a high current density leading to their erosion and consequently to a contamination of the arc by the impurities.
2. The magnetic field makes the separation of the electrodes possible. As the magnetic field lines rapidly diverge outside the coils, where the electrodes are to be, the plasma has to be guided

from the electrodes to the high magnetic field region.

3. The guidance is provided by glass funnels which are attached to the outside of the electrodes. The funnels follow the magnetic flux tube which has the same diameter at the position of the electrodes as the electrodes themselves. In this report this flux tube will be called the distinguished flux tube.
4. The funnels must not end in too high a magnetic field, because the ion mass currents flowing radially outwards at the funnel ends must not be hindered.
5. When the funnel configuration is symmetrical with respect to the center of the coil configuration ($z = 0$), the arc does not rotate in the plane of symmetry (see Chapter 1, section 1.2). The arc rotational symmetry is better when it rotates fast. A fast arc rotation is provided by an asymmetric funnel configuration. The amount of funnel asymmetry was chosen on the basis of the author's judgement.
6. In order to bring the magnetic field coils as chose together as possible and still see the whole radial extent of the arc, the window tubes were flattened in the section between the outside and inside diameter of the coils.

7. Glass windows for observation along the axis were made at the end of the discharge tube. These windows, protruding a few centimeters into the discharge tube, also prevented a high concentration of current density at the center of the electrodes.

The discharge tube, the coils and the magnetic field lines are shown in Figure 2.2.

### 2.2.2 Plasma Current, Filling Pressure, Timing

A square current pulse 200 μsec long was produced by discharging a 20 kV, 25 kJ capacitor bank through a matching resistor. The capacitors in the bank were connected in the usual way as a lumped delay line. The switching device was an NL 1036 ignitron (rated at 15 kV, 35 kA) equal to those used for the triggering of the magnetic field capacitor bank. The plasma current was adjustable to a maximum of 5 kA by changing the charging voltage of the capacitor bank.

The initial plasma development was aided by a glow discharge, connected in parallel with the main discharge. An alternative way, using a 1.6 μF capacitor, charged to 15 kV and discharged just before the main pulse, was equally successful in preionizing the plasma.

The discharge was operated at a filling pressure of 3 torr helium. Tests at higher and lower filling pressures did not lead to satisfactory plasmas. At filling pressures much higher than 3 torr the condition. $\omega_e \tau_e >> 1$ is not any more satisfied and the magnetic field has little effect on the plasma. At much lower pressures too small an electron density is obtained.

The timing of the discharge with respect to the magnetic field is shown in Figure 2.3. Since the period of the magnetic field was 2.65 msec (section 2.1) the plasma was initiated 540 μsec after the start of the

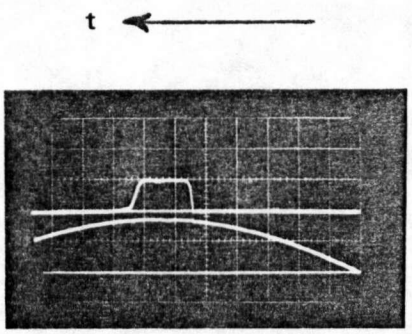


Figure 2.3 Timing of the plasma with respect to the magnetic field. Upper trace: Plasma current. Lower trace: magnetic field . Time: t = 100 μsec per division.

magnetic field. It can be seen from Figure 2.3 that the magnetic field was approximately constant during the arc discharge.

The plasma properties are analyzed in the succeeding chapters.

# CHAPTER 3

# TIME RESOLVED SPECTROSCOPY

Time and radially resolved spectroscopy provides a method for the measurement of the temperature and electron density. Usually the temperature can be determined by measuring the intensity ratio of two spectral lines belonging to different ionization stages. For helium these two lines belong to the spectrum of neutral and once ionized helium. The electron density is usually measured from the Stark broadening of the spectral lines of ionized and neutral helium.

In this chapter the spectroscopic measurement of electron density and temperature is described. Two helium lines were investigated: He I 4471 Å and He II 4686 Å. The electron density was determined from the half width of the He I 4471 Å line and the temperature from the intensity ratio of the two lines.

The results are presented and discussed in Chapter 6 together with the electron density and temperature measured with other methods.

## 3.1 Theory

In this experiment a pulsed highly inhomogeneous and to a good degree cylindrically symmetrical source of radiation was analyzed. Due to this complexity the arc spectrum had to be resolved threefold: in time, space and wavelength. In side-on observations the spectral lines have to be Abel unfolded (section 3.1.1). In such a case it is most convenient to record the spectra on a spectrographic plate, thus providing a radial and wavelength resolution with the time as a parameter.

Due to the short duration of the plasma under investigation a high temporal resolution was needed, leading to short exposure times of the plates. As the response of a photographic plate depends on the energy per unit area received by the plate, short exposure times require a high intensity of incident light. This was to some extent provided by using relatively wide slits of the detecting instruments: the spectrograph and microdensitometer. Wide detector slits however are not desirable for the half-width measurement of the spectral lines. Often, the recorded line profiles have to be deconvoluted with the instrument profile (section 3.2.3).

When the temperature is determined from the intensity ratio of two spectral lines, wide slits can be used. It has been shown [14] that the intensity ratio does not depend on the slit width when the product of the

spectrograph entrance slit width and the spectrograph dispersion (Å/mm) becomes much larger than the line halfwidth. For such wide slits the energy density distribution, recorded by the plate, is flat-topped and its maximum is proportional to the line energy. By taking a single measurement of the plate density at the center of the flat-topped distribution for each line, the ratio of their total intensities can be determined. It is therefore advantageous to use wide slits for temperature measurements. However, too wide slits must not be used, because the plate energy due to the continuum radiation grows proportionally with the slit width.

For the line intensity measurements the plates must be calibrated due to their nonlinear exposure response. The calibration is provided by illuminating a stepwedge with a standard source of continuum radiation, and then projecting the stepwedge onto the spectrograph entrance slit. A set of bands of different density is recorded by the plate. As they are produced by known exposures, the H-D curve of the emulsion can be constructed. This is sufficient for relative intensity measurements.

### 3.1.1 Abel Unfolding of Spectral Lines

The spectroscopic measurements, used in this experiment to obtain the radial distributions of electron density and temperature, required a knowledge of the

emission profile for each chosen spectral line at various local points in the plasma. In side-on observations the intensity profiles integrated along the line of observation are recorded. For cylindrical symmetry and an optically thin plasma it is possible to relate the observed intensity profiles $i_{\lambda_0}(y, \lambda)$ of a spectral line to the local emission profiles of the same line $\varepsilon_{\lambda_0}(r, \lambda)$ through the integral:

$$i_{\lambda_0}(y, \lambda) = 2 \int_y^{r_0} \frac{\varepsilon_{\lambda_0}(r,\lambda) r dr}{(r^2 - y^2)^{1/2}} \qquad (3.1)$$

where

$\lambda_0$ = central wavelength of the profile

$y$ = distance of observation line from the arc center

$r_0$ = arc radius

$r$ = cylindrical coordinate.

The emission profiles are obtained by the well known Abel transform [15]:

$$\varepsilon_{\lambda_0}(r,\lambda) = -\frac{1}{\pi} \int_r^{r_0} \frac{i_{\lambda_0}'(y,\lambda) dy}{(y^2 - r^2)^{1/2}}, \qquad (3.2)$$

where (') indicates the derivative with respect to y.

The evaluation of eq. (5.14) is most easily done by a computer. In this experiment the method given by Barr [16] was used.

### 3.1.2 Spectral Line Broadening and the Electron Density

A usual way of measuring electron density spectroscopically is to deduce it from the halfwidth of Stark broadened lines.

Two spectral lines bright enough to produce a sufficient exposure of the spectrographic plates were investigated: the He II line at $\lambda$ = 4686 Å and the He I line at $\lambda$ = 4471 Å. Under our experimental conditions both lines were broadened mainly by Stark effect, Zeeman effect, and to a smaller degree by Doppler effect. Due to relatively wide spectrograph slits the instrumental broadening was also important.

Unfortunately the profiles of the line He II 4686 Å could not be used for density measurements for various reasons. At electron densities around $10^{16} cm^{-3}$ as encountered in the investigated plasma the halfwidth of the line profile arising from the Stark effect of the electric microfields is of the order of 0.5 to 1.0 Å [15]. The contribution of Doppler broadening at $8 \times 10^4 °K$ to this would be about 0.2 Å, assuming that the Stark effect produces a Lorentzian line shape. The normal Zeeman effect of this line at magnetic fields of 4.0 Teslas introduces a shift of the $\sigma$-components of $\pm$ 0.4 Å. The actual line shape is then a convolution of all these contributions. Since no theoretical calculations for combined Stark and

Zeeman broadening are available for this line an attempt at unfolding the various contributions is foiled from the outset. But even if a reasonable assumption about the effect of the different contributions was made, the evaluation would be severely hampered by the fact that for intensity reasons the instrument profile had a halfwidth of 2 Å.

3.1.2.1 Broadening of He I 4471 Å

The profile of the He I 4471 Å was used for the measurement of the electron density.

*Stark Broadening*. The broadening of the spectral line He I 4471 Å has been extensively studied theoretically by Barnard, Cooper and Shamey (BCS) [17] and other authors and experimentally by Barnard and Nelson [18];Stevenson [19] and Burgess et al. [20].

He I 4471 Å consists of 2 components: an allowed line arising from the transition $4^3D - 2^3P$ and a forbidden line due to the transition $4^3F - 2^3P$. At the electron density of $10^{16} cm^{-3}$ the peak intensity of the forbidden component just reaches the half intensity of the allowed component. The electron densities below $10^{16} cm^{-3}$ can be obtained most accurately from the halfwidth of the allowed transition. If the minimum between the allowed

and forbidden component is not smeared out (e.g. by the instrument profile) the method of using the allowed transition for the electron density measurements can be extended up to the electron density of $3 \times 10^{16} cm^{-3}$ (Fig. 3.1).

*Doppler Broadening.* The He I 4471 Å line is emitted strongly only from the regions with temperatures ranging up to 50.000°K. At 50.000°K the Doppler halfwidth is 0.35 Å. The measured halfwidths were between 2 Å and 5 Å. The Doppler broadening was estimated to contribute less than 0.2 Å to the line halfwidth if convoluted into the theoretical profile and was neglected in our measurements.

*Zeeman Broadening.* The Zeeman splitting of the line He I 4471 Å is complex, particularly in the presence of broadening by Stark effect. The combined Zeeman and Stark splitting has been investigated by Deutch et al. [21] and the combined Zeeman and Stark broadening by Deutch [22].

The combined splitting of the lines depends on the angle between the electric field $\vec{E}$ and the magnetic field $\vec{B}$. In a plasma the electric field is due to the ions surrounding the radiating atoms and is statistically distributed. The combined broadening is calculated by averaging over the ion microfield distribution $W(\vec{E})$. The

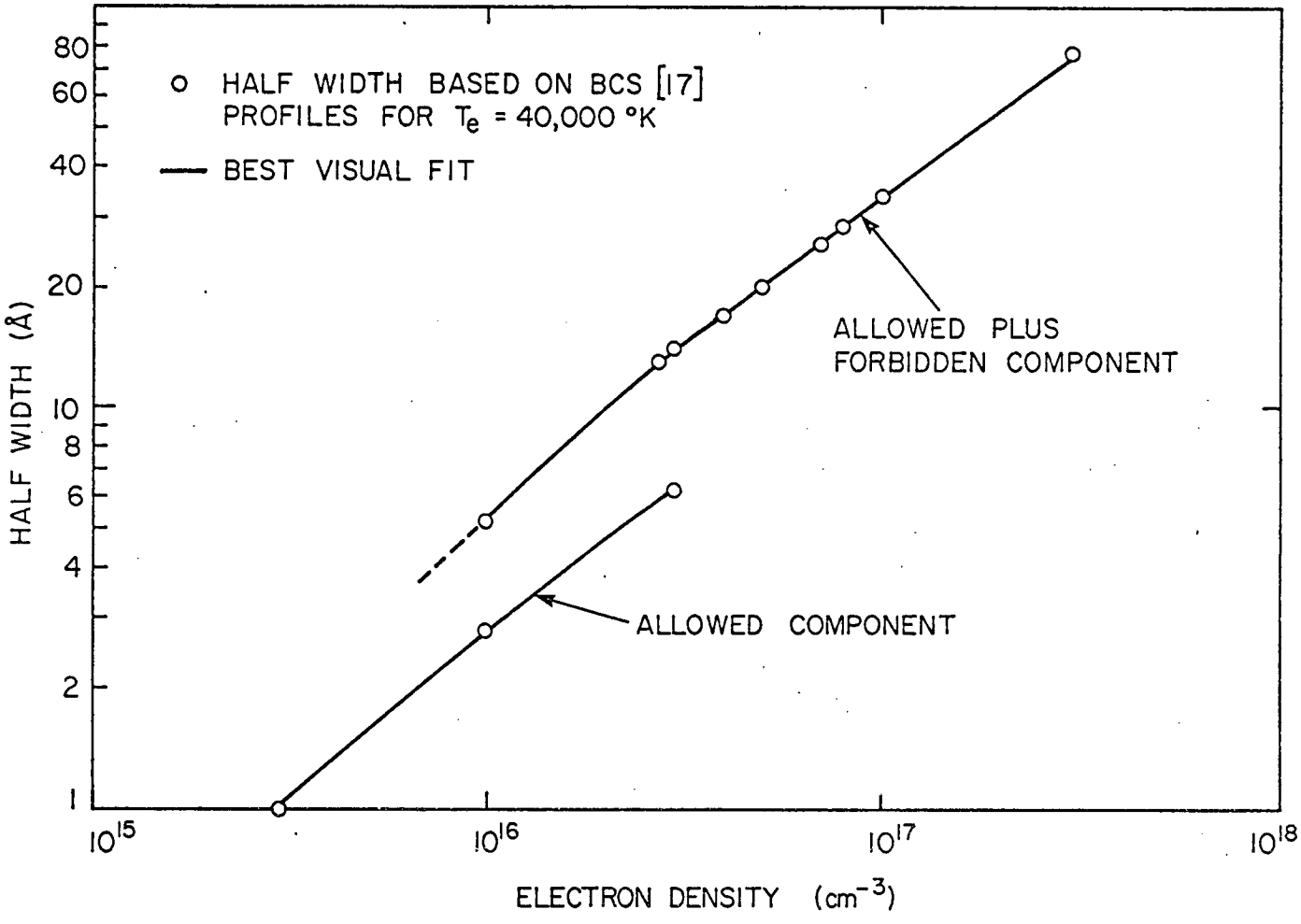


Figure 3.1 Halfwidth of the line He I 4471 Å versus electron density.

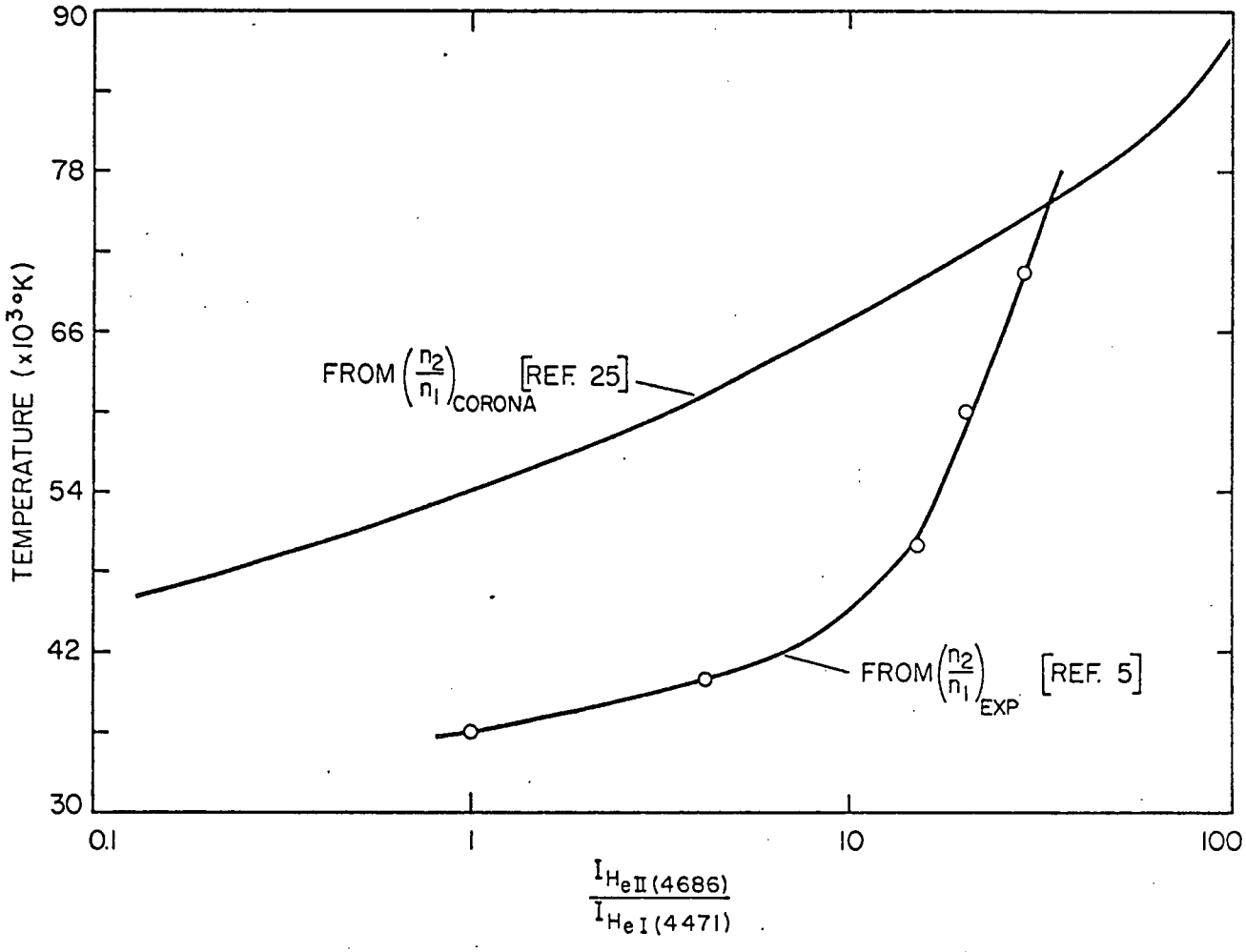


Figure 3.2 Ratio of intensities of two helium lines versus temperature.

calculations are possible if $W(\vec{E})$ is not affected by the magnetic field. This is true as long as the electron Larmour radius $r_L$ remains much larger than the Debye length $L_D$.

$$\frac{r_L}{L_D} = 4.5 \times 10^{-10} \frac{n_e^{1/2}}{B} , \qquad (3.3)$$

where B is in Teslas and $N_e$ in $m^{-3}$. The ratio (3.3) is about 10 for the plasma investigated here and the theoretical results of Deutsch [22] can be used.

The main effect of the magnetic field for the observation perpendicular to the magnetic field is an asymmetry of the line profile. The comparison of a line profile of He I 4471 Å calculated in reference [22] for the combined Stark and Zeeman broadening (B = 7.0 T $N_e = 5 \times 10^{16} cm^{-3}$) and Stark broadening only at the same electron density showed no difference in halfwidths. The plasma parameters in this experiment (B = 4 T, $n_e \simeq 10^{16} cm^{-3}$) favoured the Stark effect even more. Therefore the contribution of Zeeman broadening to the halfwidths was ignored.

### 3.1.3 Line Intensity Ratio and the Electron Temperature

In this section the measurement of temperature from the line intensity ratio of He II 4686 Å to He I 4471 Å will be described. The spectroscopic measure-

ments yield the electron temperature distribution in the cooler regions of the arc at the radius 3 mm $\leq$ r $\leq$ 8 mm. Closer to the arc axis the intensity of He I line was too weak for the measurement of the line intensity ratio.

In Appendix C the intensity ratio of two spectral lines belonging to different ionization stages is calculated. Eq. (C-5) can be rewritten as

$$\frac{i_{pq}}{i_{rs}} = F(T_e) \frac{n_Z}{n_{Z-1}} \qquad (3.4)$$

The line intensity ratio is proportional to a function of electron temperature and atomic constants $F(T_e)$ and to the ratio of densities of Z times and Z-1 times charged ions. When the ion density ratio and the line intensity ratio are known the electron temperature is determined by a graphical solution of eq. (3.4).

The next two subsections deal with the calculation of the ratio $n_Z/n_{Z-1}$.

### 3.1.3.1 Static (Corona) Ionization Ratio $n_Z/n_{Z-1}$

Much effort has been put into the calculations of $n_Z/n_{Z-1}$ for helium. The interested reader is referred to the work of Mahn [23] and Mewe [24]. To calculate the ratio $n_Z/n_{Z-1}$ all the transitions, that is all population

and depopulation processes among the levels of Z-1 times charged ion have to be considered. The most important of these levels are the lower levels which are not thermally populated and for which the Saha Boltzmann equation cannot be used. The equilibrium of lower levels is maintained by collisional excitation processes and radiation deexcitation processes. This equilibrium is the well known Corona equilibrium and the corresponding equation for $n_Z/n_{Z-1}$ is called the Corona equation. In this report the Corona equilibrium will be called static ionization equilibrium, because the dynamic effects of the ion motion are neglected in it. According to this equilibrium the ratio $n_Z/n_{Z-1}$ is [25].

$$\frac{n_Z}{n_{Z-1}} = \frac{1}{2\pi\zeta^3}\,\frac{KT}{Z^4 E^{(Z)}}\,\exp\left\{-\frac{E_i^{(Z)}}{KT}\right\} \qquad (3.5)$$

where $\zeta$ is the fine structure constant: $\zeta = \frac{e^2}{4\pi\varepsilon_0\hbar c} = \frac{1}{137}$.

The ratio of He II 4686 Å to He I 4471 Å line intensities calculated from eqs. (3.4) and (3.5) is plotted as a function of temperature in Figure 3.2. On the same graph the intensity ratio is given by another function calculated from eq. (3.4), using experimental values for $n_2/n_1$ obtained in an arc similar to ours [5].

The difference between the two curves presented in Figure 3.2 is due to the dynamic behaviour of the arc, discussed below.

### 3.1.3.2. Dynamic Ionization Ratio $n_Z/n_{Z-1}$

In Chapter 1 the axial and radial flows of charged particles caused by dynamical processes in the arc were discussed. The radial velocities of charged particles were calculated in Appendix B in terms of pressure, and densities of charged particles. Here it will be shown that the static ionization formulae cannot be applied to an arc in a magnetic field, because the static ionization equilibrium is displaced by the motion of ions. Only the ion motion parallel to the direction of temperature and density gradients, that is in the radial direction, affects the ionization equilibrium. The doubly charged helium ions diffuse outwards. Because of their finite recombination (relaxation) time they increase the local density of doubly charged ions to a value higher than the static ionization density. The larger the radial velocities and the larger the ion relaxation times the more the displacement of ionization affects the ratio $n_2/n_1$.

The local balance of charged particles is given by the following equation:

$$\frac{\partial n_Z(r)}{\partial t} = I_{Z-1}(r)\, n_{Z-1}(r) - R_Z(r)\, n_Z(r) - \mathrm{div}[n_Z(r)\vec{v}_Z(r)] \tag{3.6}$$

$I_{Z-1}$ and $R_Z$ are the local ionization and recombination rate coefficients respectively. The last term of eq. (3.6) describes the loss or gain of ionized particles of species Z in a unit volume due to their outflow or inflow. A relaxation time $\tau_Z$ can be defined as the decay time of an ion density disturbance. Then from eq. (3.6) it follows that

$$\tau_Z = \frac{1}{I_{Z-1} + R_Z} \qquad (3.7)$$

The ionization and recombination rate coefficients are proportional to the electron density, but they are complicated functions of the temperature. Moreover in an inhomogeneous plasma they as well as $\tau_Z$ are functions of position. At each radius r a balance is established among the radial flow term div $(n_Z \vec{v}_Z)$, ionization term $(I_Z n_{Z-1})$ and recombination term $(R_Z n_Z)$. For a given radial ion flow the ionization ratio $n_Z/n_{Z-1}$ is determined by the coefficients $I_{Z-1}$ and $R_Z$. According to the equation (3.7) $\tau_Z(r)$ then determines, for a given velocity distribution, the deviation of $n_Z/n_{Z-1}(r)$ from its static value. The theoretical static ionization relaxation times $\tau_2$ of doubly ionized helium are represented in Figure 3.3 as a function of temperature. $\tau_2$ was calculated from formulae derived by Mahn [23] and given by Tichmann [25] in a clear form.

At moderately high temperatures between 4 eV and 8 eV which are definitely obtained in the arc in the domain of the spectroscopic measurements of electron temperature, the ionization relaxation times are large. The ions with a small radial velocity, say 10 m $sec^{-1}$ travel a path of a few millimeters before they recombine. The number of doubly charged helium ions at a given place is then much different than their number corresponding to the static ionization.

In order that the static ionization equilibrium be present in the helium arc the inequality

$$v_{2r}\,\tau_2 << 4 \times 10^{-4}\ \text{m} \qquad (3.8)$$

has to be satisfied [5]. An expression for the radial velocity of doubly charged helium ions $v_{2r}$ is given in Appendix B. The temperature and pressure gradients taken from graphs in Chapter 6 give $v_{2r} > 10$ m $sec^{-1}$. For these radial velocities the condition of eq. (3.8) is violated.

Recall equation (3.6). In a region of the arc where there are also Z-1 charged ions an analogous equation is valid for them. In a stationary case a set of two equations describing the equilibrium in a zone of mixed Z-1 and Z times charged ions is found. The two equations are:

$$I_{Z-1}\, n_{Z-1} - R_Z\, n_Z = \text{div}\,(n_Z \vec{v}_Z)$$

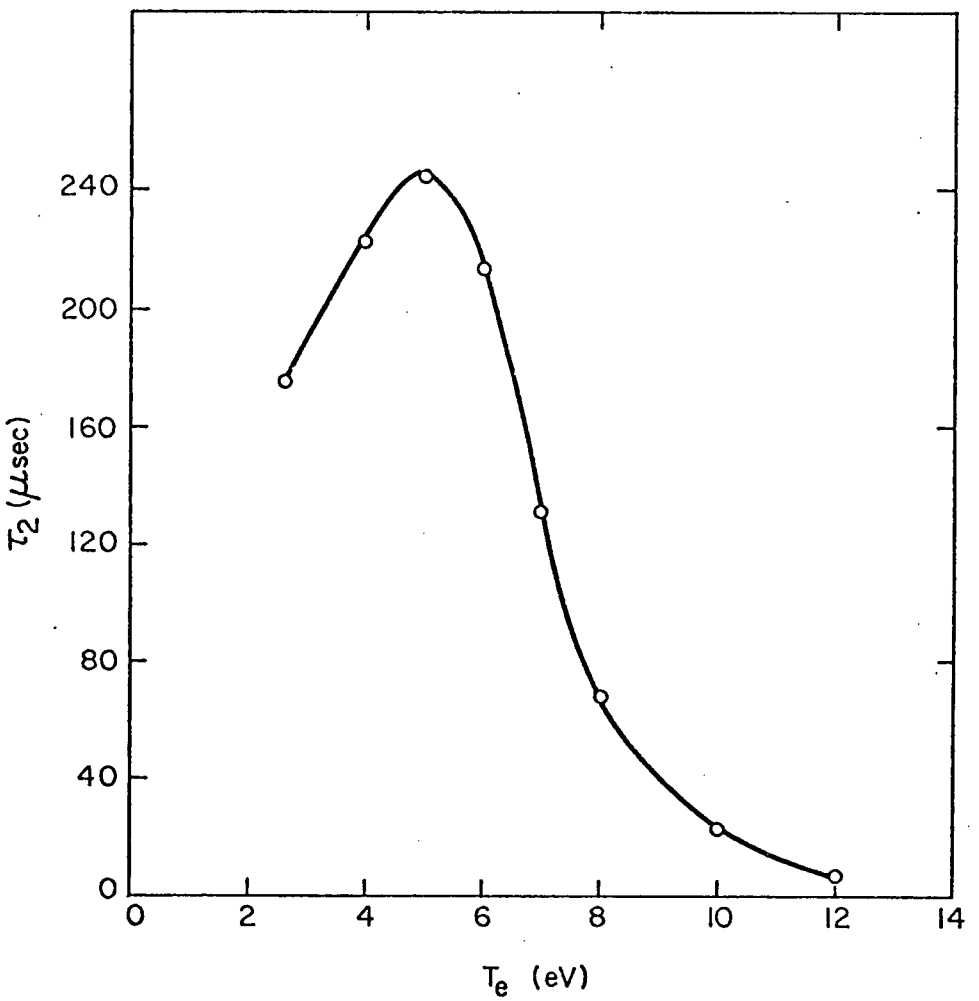


Figure 3.3 Theoretical static ionization relaxation time of doubly charged helium ions versus temperature.

$$R_Z\, n_Z - I_{Z-1}\, n_{Z-1} = \mathrm{div}\,(n_{Z-1}\, \vec{v}_{Z-1}) \qquad (3.9)$$

In the case of static equilibrium

$$I_{Z-1}\, n_{Z-1} - R_Z\, n_Z = 0, \quad \text{or}$$

$$\frac{n_Z}{n_{Z-1}} = \frac{I_{Z-1}}{R_Z} \qquad (3.10)$$

If eqs. (3.9) are solved for the ratio $n_Z/n_{Z-1}$ they become:

$$\frac{n_Z}{n_{Z-1}} = \frac{I_{Z-1}}{R_2}\left[\, 1 - \frac{\mathrm{div}(n_Z \vec{v}_Z)}{I_{Z-1} n_{Z-1}}\,\right] \qquad (3.11)$$

The second term in eq. (3.11) describes the deviation from the static ionization ratio. That term should be $<< 1$ in order that the Corona formula could be used. Unfortunately, formula (3.11) is not very suitable for the electron temperature measurements, because it contains the spatial distribution of velocities which is dependent on the temperature and pressure gradients. The Corona formula is not valid because of too large radial velocities.

Therefore the $n_Z/n_{Z-1}$ ratio must be measured for the correct determination of electron temperature.

## 3.2 Experiment

### 3.2.1 Optical System

The optical system for the time resolved spectrography (TRS) is shown in Figure 3.4.

The arc center was projected by lenses $L_1$, $L_2$, and $L_3$ onto the entrance slit of an f/12 smear camera (S.C.) [26] so that the apertures of the camera and lenses were matched. The radial extent of the field of view was determined by the size and position of the entrance pupil. The size of the entrance pupil was dictated by the diameter and length of the window tube.

In the exit plane of the smear camera a mirror was mounted to reflect the beam through lenses $L_6$ and $L_7$ onto the spectrograph entrance slit. The aperture of the spectrograph (f/6.3) was again well matched with the apertures of the smear camera and the arc-smear camera optical system. Stop 1 assured that the arc light did not overflow the spectrograph mirror and stray the light in undesired direction in the spectrograph.

The magnifications of the arc-smear camera optical system and the smear camera-spectrograph optical system were 1.4 and 0.54 respectively; the total magnification was 0.8.

The smear-camera (S.C.) served 2 purposes:

Figure 3.4 Optical system for time resolved spectroscopy and photography.

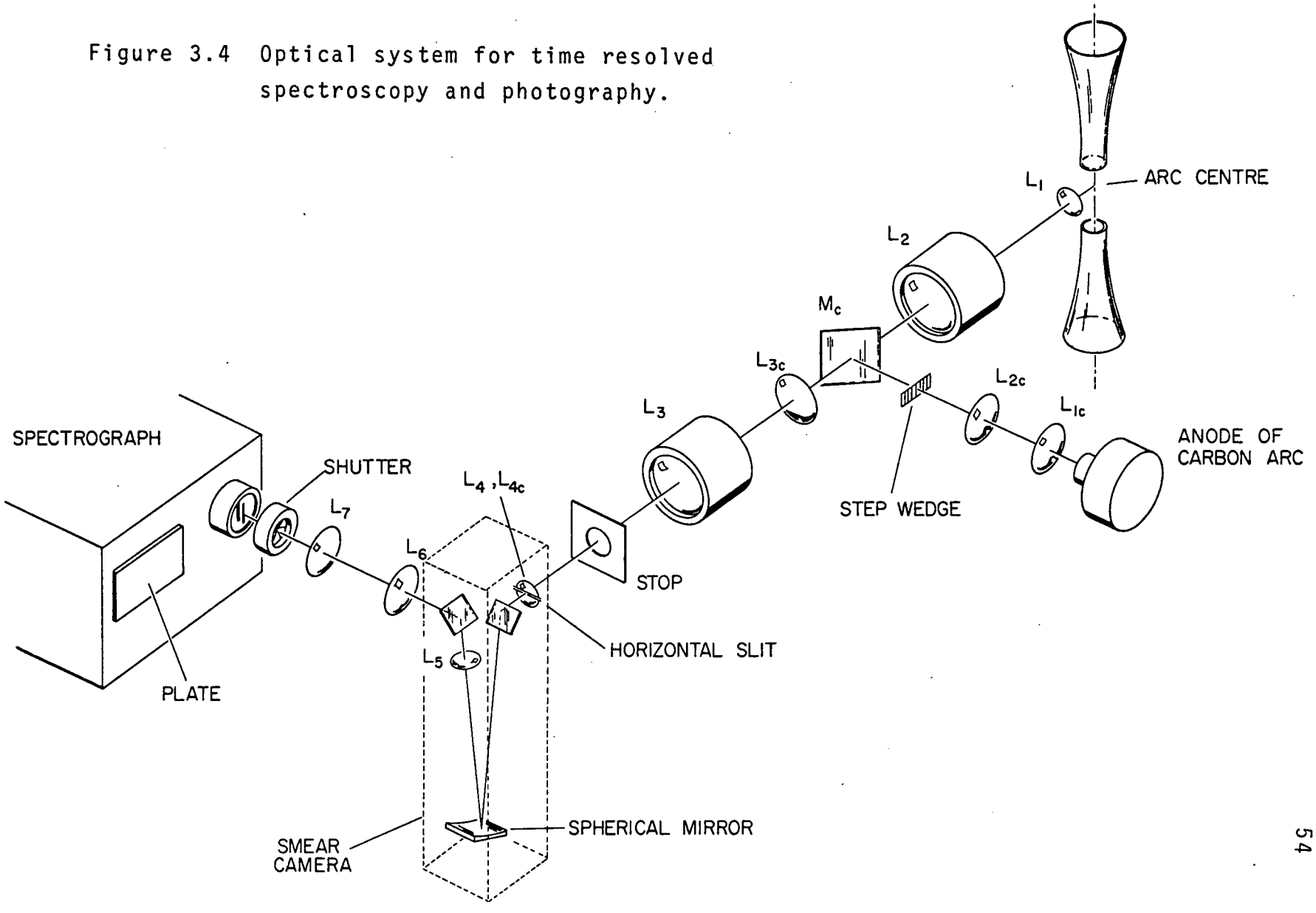

1. time resolved photographic study of the arc, and
2. a shutter for time resolved spectroscopy.

For the time resolved photographic study of the arc a conventional camera was mounted at the exit slit of the smear camera. The same arc - S.C. optical system was used as in TRS.

In TRS the beam of the arc light entering the entrance slit of the S.C. was projected onto the spectrograph entrance slit 122 or 150 μsec after the initiation of the arc. This time was determined by replacing the mirror on top of the S.C. with a Polaroid camera. From the known position of the beam in the smear camera exit plane at the time when it swept the spectrograph entrance slit, the instant of exposure was determined by studying the streak photographs. The reproducibility was checked and the error in timing was established to be less than 10 μsec.

The plate exposure time, for a given optical setup, is inversely proportional to the S.C. sweepspeed* and proportional to the combined width of S.C. plus spectrograph entrance slits. The maximum exposure time of 14-17 μsec was thus limited by the lowest S.C. sweepspeed of 0.022 cm/μsec and the necessity to use a relatively narrow spectrograph slit. So short an exposure time limited the spectroscopic investigation in this experiment to the

*The sweepspeed is the speed of the entrance slit image in the exit plane.

study of the strongest He II and He I lines, but provided a very good temporal resolution.

The width of the S.C. entrance slit also determines the spatial resolution along the axis of the arc. The spatial resolution of spectroscopic measurements was 4 mm.

For the measurement of the relative intensity distribution of spectral lines each plate has to be calibrated, in other words, the exposure response of the plate has to be found. The optical system for the calibration is shown on Figure 3.4. The standard light source is a Spindler and Hoyer carbon arc. When the arc carries a current of about 10 A the arc anode radiates like a black body at 3800°K [27].

The arc anode is projected by lenses $L_{1C}$ and $L_{2C}$ onto a Hilger F 1273 neutral density stepwedge filter. The 7 fold magnification of the arc anode image on the stepwedge assured a uniform illumination of the stepwedge. The stepwedge was projected onto the entrance slit of the S.C. and from there onto the spectrograph entrance slit.*

The S.C. served as a beam chopper for the exposure of the plates by the carbon arc. In order to ensure a stable operation the arc was run for several minutes. The needed exposure time was only about 15 μsec long, i.e., of the same order of magnitude as the exposure time for the helium arc. This is why the carbon arc light was chopped by the S.C. and shuttered by an ordinary camera

*The stepwedge had 7 filter steps. In order to get more points for the H-D curve, narrow strips of neutral density filter were mounted on the spectrograph plate holder so that they covered a strip of the stepwedge image in the vicinity of the lines to be analyzed. This way 21 points for each stepwedge curve were obtained.

shutter put in front of the spectrograph slit (see Figure 3.4).

At the instant of exposure the S.C. was rotating with a period of 13 msec . Without the shutter the plate would be exposed too many times during several minutes of the arc operation. By opening the shutter for 1/3 or 1/2 of a second the carbon arc exposed the plate only 15 or 40 times for about 18 μsec each time.

All these precautions were necessary in order to avoid reciprocity failure of the plate emulsion. Theoretically there should be no reciprocity failure for the exposure times as short as used in this experiment [28] so that small differences between the exposure times of the carbon arc and the helium arc should not matter.

The intermittency effect is another possible source of failure of the photographic emulsion [29]. This failure arises due to the fact that the emulsion reacts to a large number of short exposures equally as if it would be exposed by only one exposure for the time equal to the sum of all short exposure times. As long as the number of exposures is kept below about 100 the intermittency effect is absent.

One limitation was imposed by the spectrograph itself due to its astigmatism. Lines perpendicular to the entrance slit could not be focused along the whole length of the plate. Because of that the two lines used

for the temperature measurement had to be relatively close together if radial resolution was to be possible. The spectrograph was then focused in their vicinity so that the smearing of the lines and stepwedge due to misfocusing was negligible.

### 3.2.2 Plate Analysis

The plates were analyzed on a Grant Spectrum Line Measuring Comparator. This comparator records 3 co-ordinates: X = position that corresponds to wavelength, Y = position that corresponds to radial spread of the line, and the plate transmission. The X position and plate transmission were recorded automatically on an IBM 526 card punch upon a push of a button. The Y position was punched manually.

Ideally the comparator slit should be as wide and as long as possible to average the transmission reading over a large number of emulsion grains. Also the Comparator is more stable at lower sensitivity (for a larger slit area a lower sensitivity is needed to give the same output signal). In practice, however, a compromise had to be made, because a high radial and wavelength resolution was desired. The Comparator was used at maximum sensitivity and at maximum magnification (20 times). The slit length, oriented along the spectral line, was 10 mm long, corresponding to a length of 0.5 mm on the plate. Because the arc-sepctrograph

magnification was 0.8, the radial resolution of the measurements was about 0.6 mm. For most readings the Comparator slit width was 0.6 mm corresponding to 0.3 Å on the plate.

Each line was scanned in the X direction at constant Y. Then the Y coordinate was changed by 0.5 mm and the X scan repeated. The number of such profiles was between 10 and 20 for each line, ensuring good accuracy for Abel unfolding.

The data of the stepwedge and the line profiles were then processed by an IBM 360 computer. The outputs were the Abel unfolded spectral line profiles with the radius as a parameter. The line halfwidths and the intensity ratios were then determined manually, because some judgement for the magnitude of the continuum and because of eventual scatter of the profile points was necessary.

### 3.2.3 Interpretation of Spectral Line Intensities

Due to low exposure times, necessitated by the desire for good temporal resolution, the slits used were so wide that for halfwidth measurements the measured line profiles should have been deconvoluted from the instrument profiles. However instead of deconvoluting the line shapes the theoretical intensity distribution of He I 4471 Å (BCS) was convoluted with the instrument profile.* The latter was a trapezoid with the bases of 2.3 Å and 1.7 Å (2 Å due to the spectrograph, 0.3 Å due to microdensitometer. The halfwidth of the allowed component of the convoluted profile was then plotted versus the halfwidth of the allowed component of the true theoretical profile of He I 4471 Å. The convoluted profiles corresponded to the measured profiles. The halfwidths of the true profiles were then determined from the halfwidths of the measured profiles by interpolation in this graph.

For temperature measurements the ratio of doubly to singly charged helium ions $n_2/n_1$ has to be determined experimentally (see section 3.1.3). For this, two measurements have to be done, e.g.: (1) the intensity ratio of

---

*I thank Dr. A.J. Barnard for convoluting the profiles.

two spectral lines (measured in this experiment) and (2) the intensity ratio of a helium line to continuum. The latter measurement was impossible in this experiment, because of too short exposure times. Instead two approximations for $n_2/n_1$ were used: the Corona equation and an experimental curve, giving $n_2/n_1$ as a function of temperature, obtained in a similar arc by Bergstedt [5].

The temperature and pressure gradients in the arc discussed here were about the same as in that investigated by Bergstedt. As the radial velocity and consequently the ionization ratio depend on these gradients, Bergstedt's ratio of $n_2/n_1$ is considered a better approximation to the conditions in this experiment. Thus two curves for the temperature were obtained by a graphical solution of the equation (3.4).

A wide spectrograph entrance slit (1 mm) was used for temperature measurements as well as a narrow slit (0.2 mm) which was used also for the electron density measurements. In the former case the maximum intensity of the flat-topped profiles was measured whilst in the latter case the profiles had to be integrated graphically.

### 3.2.4 Photographic Study of the Arc

The simplest yet very informative study of the arc consisted of time resolved photography with a smear camera. In this experiment the camera was used at its slowest speed. The optical setup was the same as that of the arc-smear camera system of the time resolved spectroscopy, which is described in detail in section 3.2.1 (Figure 3.4).

The arc was analyzed at various currents between 1.0 and 5.0 kA, various filling pressures between 0.5 and 30 torr and a few values of magnetic induction ranging up to 4.0 Teslas (at z = 0).

For each set of parameters pictures were taken in full plasma light and in the light of the line He II 4684 Å. For the latter an interference filter was used with maximum transmission at a wavelength of 4686 Å and a passband of 15 Å. Both methods complemented each other. The He II line was emitted mostly from the hotter regions of the arc close to the discharge axis.

The pictures taken in He II light therefore show the diameter of the hot core of the arc. The pictures exposed to full plasma light showed mainly the cooler regions of the arc from which mostly He I light was emitted. They show the total spread of the arc column.

Stationary and unstationary rotation of the arc was also studied. The results are presented in Chapter 6, section 6.1.

# CHAPTER 4

# LASER INTERFEROMETRY

Laser interferometry is a simple method for the study of the arc at varying values of plasma current, magnetic field and filling pressure.

The interferometer used in this experiment was of the Fabry-Perot type previously used in this laboratory by Funk [30], Stevenson [19] and Preston. A greatly improved and sophisticated Fabry-Perot interferometer has been developed by Funk [30] and Preston and Curzon [31]. For this experiment it was decided to use the conventional arrangement because of its simple construction and alignment.

## 4.1 Theory

The refractive index of the cavity changes when a plasma is introduced in the interferometer. The refractive index n of a plasma depends on electron density $n_e$. In a magnetic field B parallel to the laser beam the refractive index is given by

$$n^2 = 1 - \frac{\omega_p^2}{\omega(\omega \pm \omega_e)} \quad , \qquad (4.1)$$

where

$\omega_p$ = plasma frequency

$\omega$ = laser frequency

$\omega_e$ = electron cyclotron frequency.

For magnetic fields of our interest (up to 5 Teslas) and a He - Ne laser the inequality $\omega >> \omega_e$ is satisfied. Making further use of inequality $\omega >> \omega_p$, one can write for equation (4.1):

$$n = 1 - \frac{e^2 n_e}{2\varepsilon_0 m_e \omega^2} \quad , \qquad (4.2)$$

where $n_e$ is the electron density and the other symbols have their usual meaning.

A laser beam passing through a region of length L with a refractive index n(z), changing along the laser beam, experiences a total phase change of $\delta$:

$$\delta = \frac{2\pi}{\lambda} \int_0^L [n(z) - 1]dz \qquad (4.3)$$

Knowledge of the plasma length L and of the variation of electron density along the resonator axis allows us to

determine the electron density from the modulated intensity of the laser beam. Usually the electron density is assumed constant along the whole length of the plasma. A phase change of $2\pi$ or an equivalent optical path length change of $\lambda/2$ then corresponds to a change in electron density of

$$\Delta n_e = \frac{2m_e \varepsilon_0 \omega^2}{e^2 L} = \frac{1.14 \times 10^9}{\lambda L} \text{ cm}^{-3} \qquad (4.4)$$

where $\lambda$ and L are both in meters. The number of maxima or minima in the modulated laser beam is the measure of the electron density.

## 4.2 Experiment

The Fabry-Perot resonant cavity is formed between the exit reflector of the laser and a mirror outside the laser cavity. The experimental arrangement is shown in Figure 4.1. The rotatable plexiglass plate is used for radial scanning of the arc. The 1 mm diameter stop limits the cross section of the beam to give a desired spatial resolution. The presence of other components is obvious.

A change of the optical path length in the external cavity changes the phase between the two laser beams and the output intensity is modulated. The optical path length changes due to two main reasons: vibrations of the mirrors and changes of refractive index of the cavity.

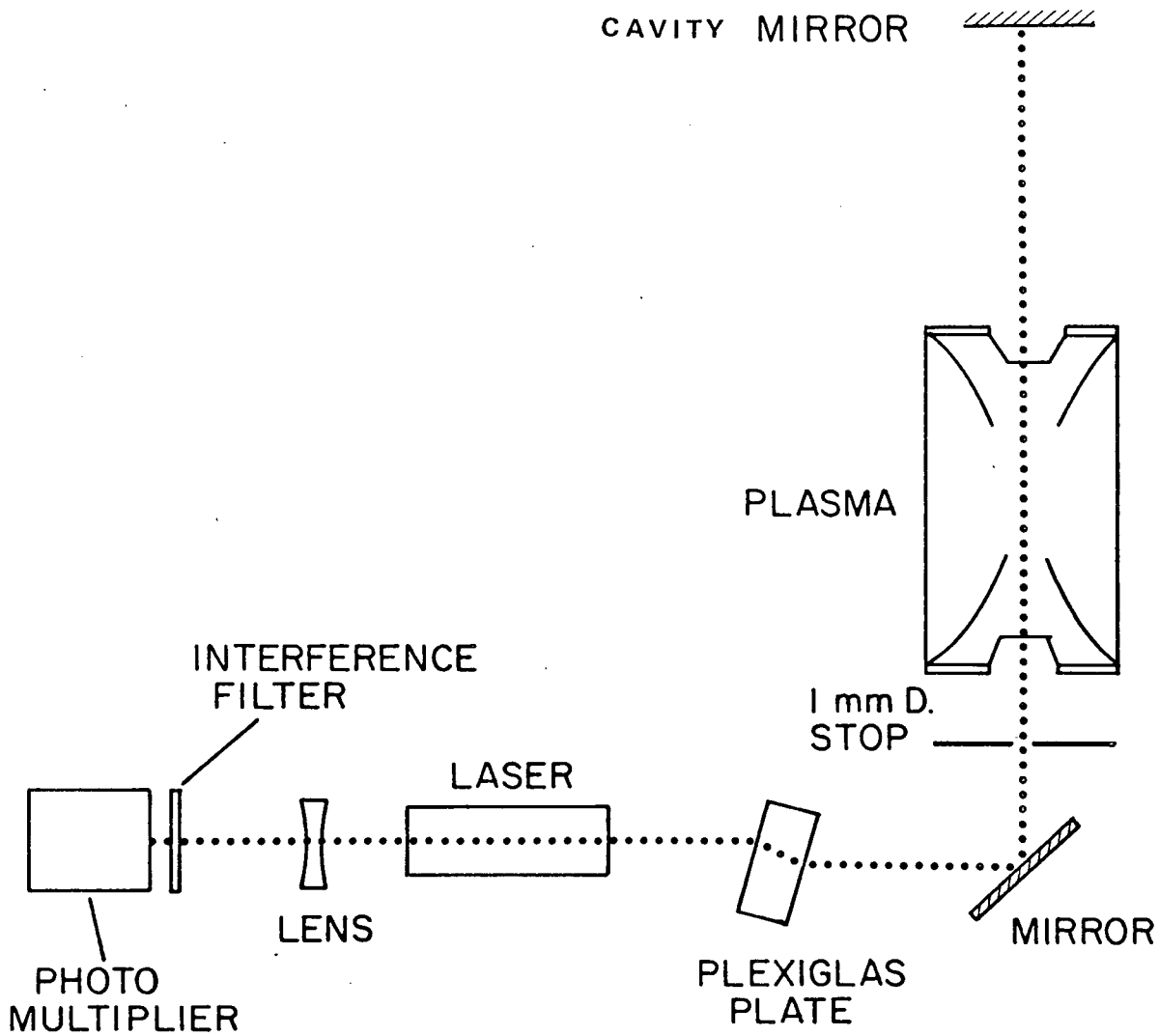


Figure 4.1 Laser interferometer.

The vibration of the mirrors has to be reduced as much as possible, so that it does not contribute to phase changes of the beam. For this reason no component of the interferometer was attached to the table on which the discharge was fixed. Also the vacuum pump was shut off while the fringe pattern was being taken.

Some vibrations of the Fabry-Perot cavity remain in spite of all precautions. These vibrations make the initial or final phase of the interference fringe pattern uncertain by $\pm\pi$ or half of a fringe [30]. How this ambiguity was avoided is described in the next section.

## 4.3 Interpretation of Interferograms

The interpretation of interferometric data is based on the assumption that the plasma is homogeneous along the laser beam. A few other problems make the measurements more difficult, e.g., the uncertainty of the initial phase, the impossibility of predicting the time derivative of the electron density, the unstationary behaviour of plasma at the start of the discharge etc.

### 4.3.1 Plasma Homogeneity

The plasma discussed in this report has a complicated geometrical configuration (see Figure 3.1, Chapter 3), therefore it was not automatically assumed that the electron

density was constant along the beam path. E.g., the electron density might have axial gradients, because the magnetic field and the arc cross section vary along the arc axis.

For this reason the interferometry was used only to measure the relative radial distribution of the electron density. The absolute values of the interferometric electron densities were obtained by fitting the interferometric electron density profile onto the electron density profile obtained from spectroscopical data. The fitting was done at the radii at which both methods were most reliable. Thus a calibration constant for the interferometric electron density profiles was obtained. One fringe corresponded to a change of electron density of $0.34 \times 10^{16} cm^{-3}$. The electron density profiles are given in Chapter 6, section 6.1.2. The possible plasma inhomogeneity is discussed in Chapter 6.

### 4.3.2 Instability of Fringes Due to Unstationary Behaviour of Plasma

In Chapter 1, section 1, it was mentioned that the plasma is unstationary at the beginning of the discharge due to unavoidable radial component of the electric current density. The consequence of this unstationary behaviour was that the fringes were unstable at the beginning of the discharge, showing rapid oscillations that could not be well resolved. A few typical oscillograms are shown in Figure 4.2. Of primary interest in this experiment was

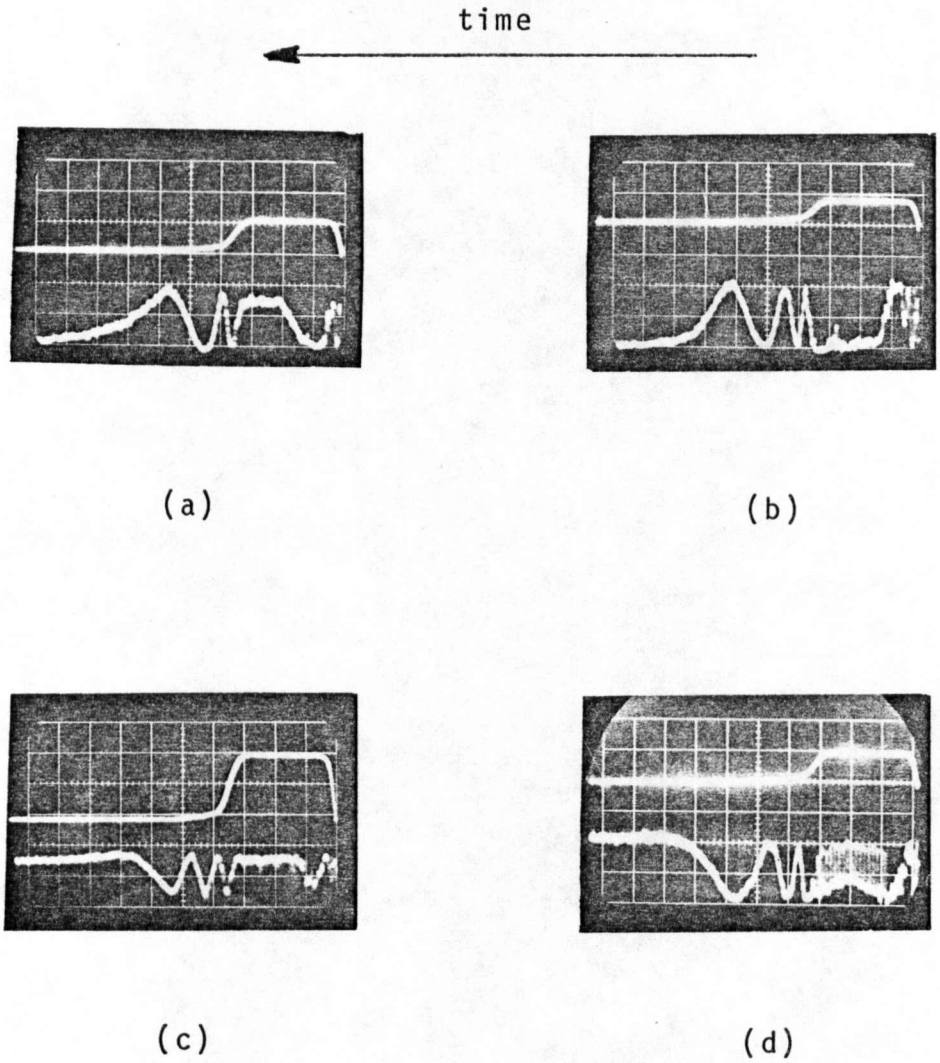


Figure 4.2 Laser interferograms. Data: $B_z$=4.0 T, filling pressure $p_f$=3 torr; plasma current: a) 1.35 kA, b) 2.0 kA, c) and d) 2.7 kA. Scales: t=50μsec/div; lower trace (fringes), 0.05 V/div; upper trace (plasma current); a) and c) 1.35 kA/div, b) and d) 2.7 kA/div.

the electron density towards the end of the constant part of the plasma current (at t ≃ 150 μ sec after the start of the current). The plasma was stationary at that time. Later the electron density reproducibly decayed to zero.

To avoid this difficulty, the fringes were counted from the end of the plasma pulse.

At currents higher than 2.7 kA the plasma was unstationary during the whole current pulse causing a rapid oscillation of interference fringes. Information about the arc rotation was obtained from such interferograms. The results are given in Chapter 6, section 6.1.

### 4.3.3 The Ambiguity of the Final (Initial) Phase

The ambiguity of final phase was partially avoided by taking enough photographs and analyzing only those that ended at a peak transmission or close to it. Such photographs were easy to identify provided that the fringes had an approximately constant amplitude (see Figure 4.2). The number of fringes was thus identified to within 1/4 of a fringe.

### 4.3.4 Sign of the Time Derivative of the Electron Density

A disadvantage of a simple interferometer such as the one used in this experiment is the impossibility of predicting the sign of the time derivative of the electron

density. Therefore, it is very difficult to determine the boundary between increasing and decreasing electron densities. In the plasma discussed here this was no problem. The fringes were counted back from the end of the plasma pulse, i.e., in the range of decreasing electron densities. The electron density at the time $\approx$ 150 µsec after the start of the current pulse was measured. As the electron density between the times of 80 µsec and 150 µsec was approximately constant, it was relatively easy to establish the fringe reversal.

# CHAPTER 5

# LASER SCATTERING

In recent years laser scattering has become a standard diagnostic technique for analyzing laboratory plasmas. The development of Q-switched lasers and photomultipliers highly sensitive at the ruby wavelength has greatly facilitated the detection of the scattered light. A considerable advantage of laser scattering over other diagnostic techniques lies in the fact that the measurements can be made with high spatial and temporal resolution. It also gives information about a wide range of plasma properties and parameters such as electron and ion temperatures, electron density, fluctuations, velocity distribution, drifts and waves, etc. This information is obtained from the spectral distribution and total intensity of scattered light.

## 5.1 Theory

### 5.1.1 Scattered Power and Spectral Distribution

The power scattered into a solid angle $d\Omega$ in a frequency interval $d\omega$ is given by

$$dP_s(\vec{k}, \omega)d\omega = \frac{d^2\sigma}{d\Omega\ d\omega} P_0\ dl\ d\Omega\ d\omega \qquad (5.1)$$

where

$P_s$ = scattered power

$P_0$ = incident power

$dl$ = length of the scattering volume

$\vec{k}$ = $\vec{k}_1 - \vec{k}_s$ is the scattering wave vector, given as the difference between the incident and scattered wave vectors

$\omega$ = $\omega_i - \omega_s$ is the frequency shift, given as a difference between the frequencies of incident and scattered light.

The differential scattering cross section per unit solid angle per unit frequency interval is usually expressed in terms of Thompson scattering cross section $\sigma_T$ and the form factor $S(\vec{k}, \omega)$.

$$\frac{d^2\sigma}{d\Omega\ d\omega} = \sigma_T\ S(\vec{k}, \omega) \qquad (5.2)$$

The form factor describes the spectral distribution of the scattered radiation. Its calculations have been published and discussed in many references, e.g. [32].

The spectral distribution of scattered light $S(\vec{k}, \omega)$ may best be understood in terms of the parameter

$\alpha$ defined as the ratio of scale length for scattering $k^{-1}$ and the Debye length $L_D$

$$\alpha = \frac{1}{k\ L_D} = \frac{1}{2k_i\ L_D\ \sin(\theta/2)} \tag{5.3}$$

Where $\theta$ is the scattering angle, i.e. the angle between the incident and scattered wavevectors.

The scattered spectrum can be easily calculated if the following assumptions are made: Maxwellian distribution of both electrons and ions, no collisions, Coulomb interaction energy is small compared with the thermal kinetic energy, the observation time is long compared with the period of fluctuations, and no external magnetic field. With these assumptions the frequency spectrum is given by

$$S(\omega, k) = \frac{n_e}{k} \left\{ \left| \frac{1-G_i}{1-G_e-G_i} \right|^2 F_e(-\tfrac{\omega}{k}) + Z \left| \frac{G_e}{1-G_e-G_i} \right|^2 \right.$$

$$\left. x\ F_i(-\tfrac{\omega}{k}) \right\} \tag{5.4}$$

where:

$F_e(-\frac{\omega}{k})$ and $F_i(-\frac{\omega}{k})$ are the Maxwell-Boltzmann velocity distribution functions, $F(v) = (\frac{m}{2\pi KT})^{1/2} \exp\{-\frac{mv^2}{2KT}\}$ for the electrons and ions respectively.

$$G_e(\omega) = -\alpha^2 \left[1 - f(x) + i\pi^{1/2}\, x \exp(-x^2)\right]$$

$$G_i(\omega) = -Z\left(\frac{T_e}{T_i}\right) \alpha^2 \left[1 - f(y) + i\pi^{1/2} y \exp(-y^2)\right]$$

$$x = \frac{\omega}{\omega_e}\,, \quad y = \frac{\omega}{\omega_i}\,, \quad \omega_e = \left(\frac{2k^2\, KT_e}{m_e}\right)^{1/2} = kv_e,$$

$$\omega_i = \left(\frac{2k^2\, KT_i}{m_i}\right)^{1/2} = kv_i$$

$$f(x) = 2x \exp(-x^2) \int_0^x \exp(t^2)\, dt$$

For $T_i \leq T_e$ a good approximation to equation (5.4) can be given in terms of a family of single parameter functions $\Gamma$, of one variable:

$$S(\omega, k) = \frac{n_e}{k} \left[\frac{1}{\omega_e} \Gamma_\alpha(x) + Z \left(\frac{\alpha^2}{1+\alpha^2}\right)^2 \frac{1}{\omega_i} \Gamma_\beta (y)\right] \qquad (5.5)$$

where:

$$\Gamma_\alpha(x) = \exp(-x^2) \left\{\left[1 + \alpha^2 - \alpha^2 f(x)\right]^2 + \pi\alpha^4 x^2 \exp(-2 x^2)\right\}$$

$$\Gamma_\beta(y) = \exp(-y^2) \left\{\left[1 + \beta^2 - \beta^2 f(y)\right]^2 + \pi\beta^4 y^2 \exp(-2y^2)\right\}$$

$$\beta^2 = \frac{T_e}{T_i} \frac{Z\alpha^2}{1+\alpha^2}\,, \quad x = \frac{\omega}{\omega_e}\,, \quad y = \frac{\omega}{\omega_i}\,.$$

Examination of equation (5.5) shows that the first term represents relatively wide distribution, corresponding to Doppler spread frequencies characteristic of the electron thermal motion, whereas the second term represents a much narrower spectral distribution corresponding to the ion thermal motion. It is convenient to refer to the two terms as electron and ion components of the scattered spectrum respectively. The two components are plotted in Figure 5.1 for various values of the parameter $\alpha$.

As a function of $\alpha$ the scattered spectrum changes from a Gaussian shape ($\alpha << 1$) via a flat topped spectral distribution ($\alpha \simeq 1$) to a spectrum with a distinct peak at plasma frequency ($\alpha >> 1$). In the presence of a magnetic field the scattered spectrum is modulated at cyclotron harmonics when the scattering plane is perpendicular to the magnetic field.

### 5.1.2 Fitting of Experimental Data to the Theoretical Profiles

The fitting of experimental scattering data to the theoretical profiles gives electron temperature and $\alpha$. The technique used in this experiment was originally proposed by Kegel [33]. It has been improved and computerized in this laboratory by Churchland [34] and Godfrey [35].

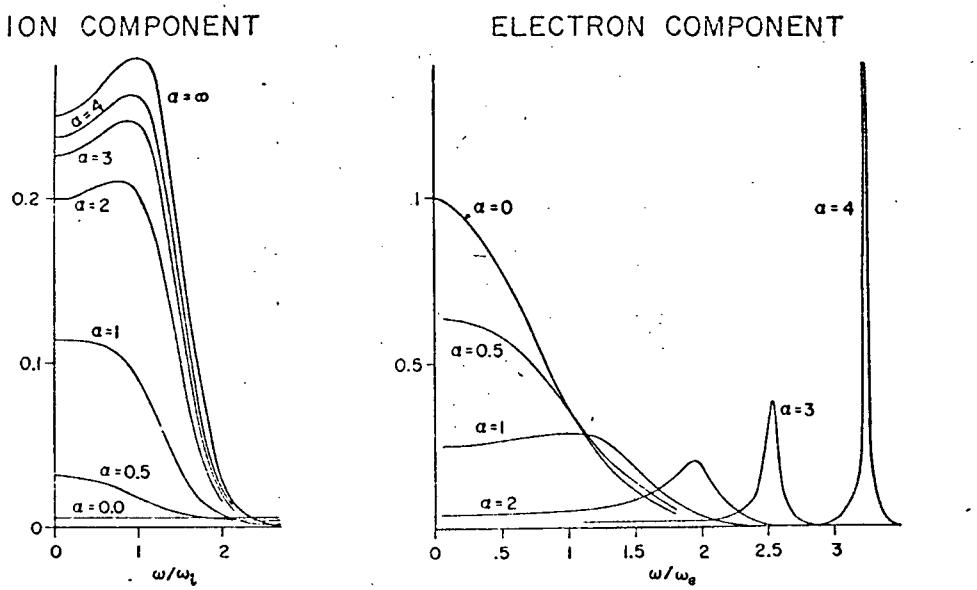


Figure 5.1 Shape of the electron and ion components as a function of parameter $\alpha$ for case $T_i = T_e$.

From eq. (5.5) it can be seen that for a given $\alpha$ the electron component of the scattered spectrum is only a function of a dimensionless parameter x.

$$x = \frac{\omega}{k\, v_e} = C\left(\frac{\Delta\lambda}{\sqrt{T}\, \sin\frac{\phi}{2}}\right) \qquad (5.6)$$

Where C is a constant for a given wavelength of the incident light and $\Delta\lambda$ is the wavelength shift.

$$\log_{10} x = \log_{10} C + \log_{10}\Delta\lambda - \frac{1}{2}\log_{10}(T \sin^2\frac{\theta}{2}) \qquad (5.7)$$

Two profiles of the same $\alpha$ have to coincide if they are normalized to x. This can be used to determine the value of $\alpha$ for an experimentally recorded spectrum.

The theoretical profiles are plotted as $\log_{10} S(\alpha, \Delta\lambda)$ vs $\log_{10} \Delta\lambda$ for a certain temperature $T_{th}$. For various $\alpha$'s a family of profiles is obtained with $\alpha$ as a parameter. The experimental profile is also plotted on the same type of graph with the ordinate $\log_{10}$ (rel. intensity) normalized to the same value as the ordinate of the theoretical profile. Then the experimental profile is fitted on one of the theoretical profiles (least square fitting can be used) by shifting the profiles horizontally and vertically with respect to each other. Thus $\alpha$ is determined.

The experimental electron temperature $T_{ex}$ is determined from the relative wavelength shift of the experimental versus theoretical curve by the formula:

$$\log_{10} \frac{T_{ex}}{T_{th}} = 2(\log_{10} \Delta\lambda_{ex} - \log_{10} \Delta\lambda_{th}) - 2 \log_{10}\left(\frac{\sin \frac{\theta_{ex}}{2}}{\sin \frac{\theta_{th}}{2}}\right) \quad (5.8)$$

Indices ex and th refer the corresponding quantities to experimental and theoretical profiles respectively.

The accuracy with which the electron density and $\alpha$ can be determined by this fitting method depends on the value of $\alpha$. For small $\alpha$'s the electron temperature is accurate and $\alpha$ is not. For intermediate $\alpha$'s the accuracy of both is about equal. For large $\alpha$'s the density can be determined accurately but the error in electron temperature is large.

## 5.2 Experiment

The magnetic field coils and the discharge vessel were designed so that the scattering plane is perpendicular to the external magnetic field and scattering angle is 90°. A scattering angle of 90° gives small $\alpha$'s. It is also the most favourable angle for reducing the stray light. The perpendicularity of the magnetic field and the scattering plane is a condition for the modulation of the scattered spectrum at cyclotron harmonics. However, in this experiment

no attempt was made to resolve the cyclotron harmonics. The scattered spectrum was used only for the determination of electron temperature and density.

### 5.2.1 Scattering Apparatus*

#### 5.2.1.1 Description

The scattering apparatus is shown in Figure 5.2. It consists of a pulsed ruby laser, an optical system that focuses the laser beam into the plasma and a detection system.

The Q-switched ruby laser consists of an oscillator with a polarizer and a Pockels cell and an amplifier (Figure 5.3b). The Pockels cell Q-switches the laser. It is charged to 10 kV until it is triggered by a coaxial spark gap (Figure 5.3a). A few nanoseconds after the spark gap breaks down, the voltage of the Pockels cell drops from 10 kV to 0 volts in about 2 nanoseconds, opens the Pockels cell and thus Q-switches the laser.

The laser beam is focused onto a pinhole of the diameter of 1.5 mm. The pinhole is imaged with an approximately one to one magnification into the center of the plasma. It was found that the pinhole reduced the stray light.

The scattering optics consists of two lenses that image the arc center onto the entrance slit of a 3/4-m

*The laser and spark gap were built and operated by Dr. J. Meyer. The whole scattering experiment was done in cooperation with him.

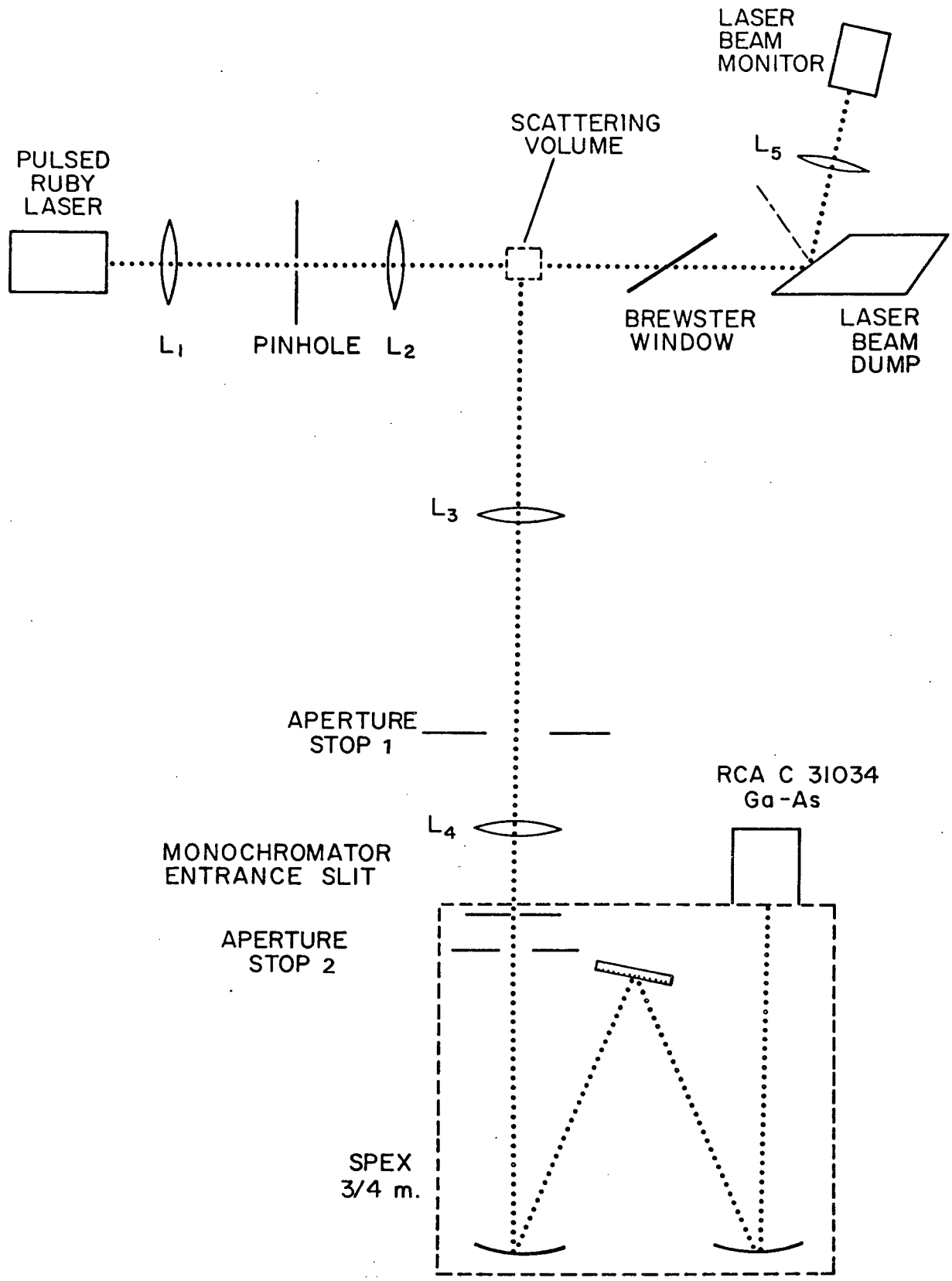


Figure 5.2 Apparatus for the laser scattering experiment.

Figure 5.3 Details of Figure 5.2 (a) Spark gap for triggering the Pockels cell (b) Pulsed ruby laser.

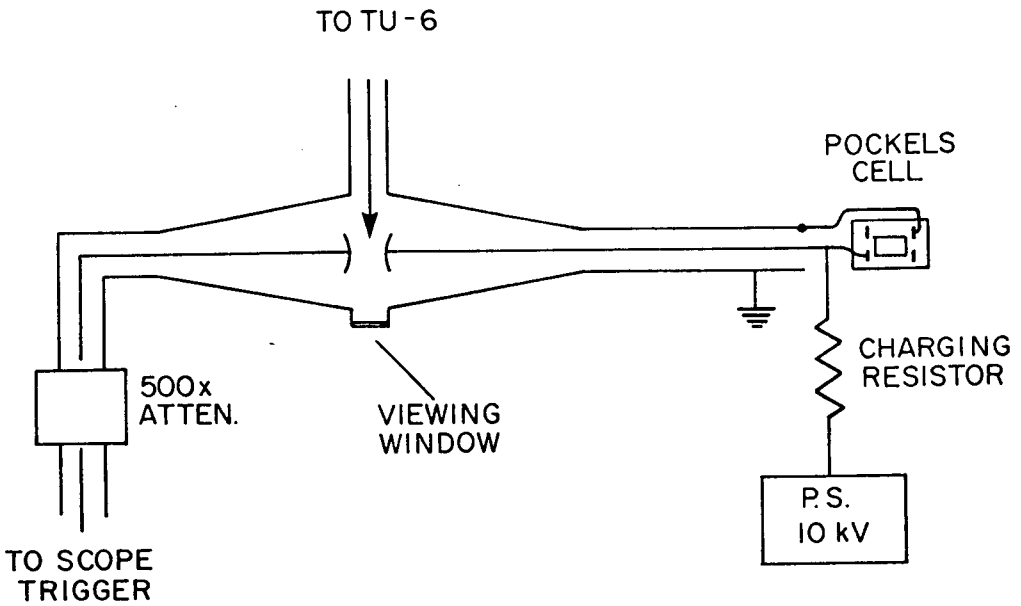


(a)

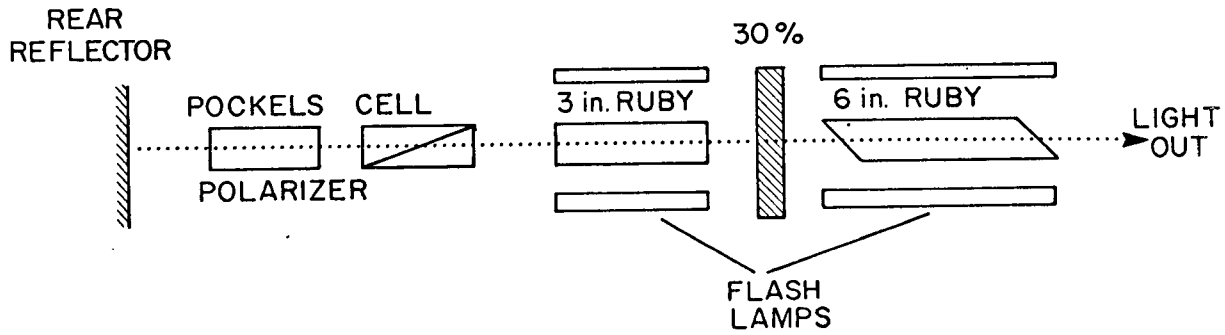


(b)

Spex monochromator. The magnification of the detection system is 0.9.

The scattering volume is thus determined by the size of the pinhole image in the plasma (1.5 mm in diameter) and by the size of monochromator entrance slit (0.8 mm wide, 1.0 mm high). The viewing solid angle was limited by stops 1 and 2 to small enough size such that no glass of the window tube was seen by the monochromator ($d\Omega = 0.5 \times 10^{-2}$ sterad).

Stop 1 prevented the light from overflowing the monochromator mirror.

The spectrally resolved scattered light was detected with an RCA C 31034 photomultiplier with a GaAs photocathode which has a quantum efficiency of 12% at 6943 Å.

The undeflected laser beam passed through a brewster window and was absorbed in a laser dump. The small part of the undeflected beam that was reflected from the dump surface was focused on a light pipe which led the light onto a monitoring photodiode.

The photomultiplier signal was recorded on a 7704 Tectronix oscilloscope simultaneously with the reference signal. The reference signal was delayed by 300 nsec with respect to the scattered signal.

The triggering circuitry and the relative timing of the components of the experiment is evident from the

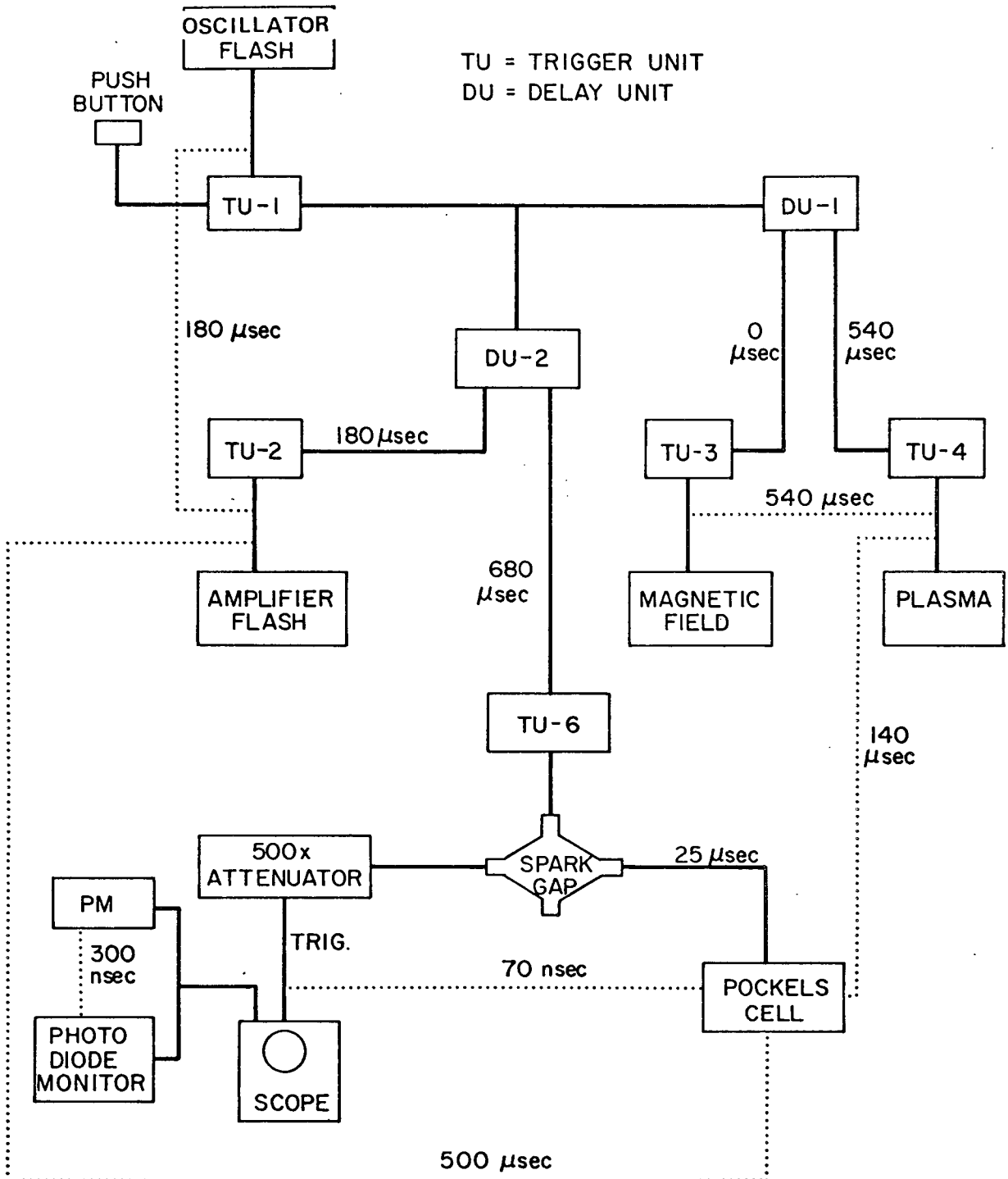


Figure 5.4 Block diagram of the triggering components and timing for laser scattering.

block diagram of Figure 5.4. The relative timing of the components that were not directly connected with cables through delay on triggering units is indicated by dotted lines.

5.2.1.2 Alignment

The optical system of the scattering apparatus was aligned with the help of two small CW lasers: one defined the arc center-pulsed laser optical axis, the other defined the arc center-monochromator axis. (The components of the pulsed ruby laser are assumed to be aligned with respect to each other). The exact location of the scattering volume was determined with a piece of film pushed into the discharge tube at approximately an angle of 45° with respect to each beam.

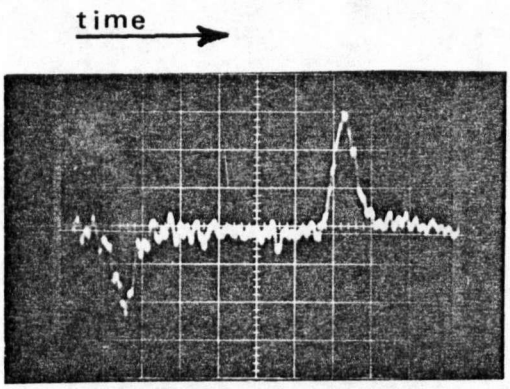


Figure 5.5 Oscillogram of the scattered and reference pulses. Horizontal scale: 50 nsec/div., vertical scale: 10 mV/div. Left: scattering pulse, right: reference pulse.

The aligning laser beams were adjusted so that they crossed each other at the arc axis (assumed to be the discharge tube center). Then a hole was punched in the film by the pulsed laser beam. That hole was focused on the entrance slit of the monochromator. The position and size of stops and pupils of the system and the viewing solid angle were determined by illuminating the spectrograph from its exit plane.

5.2.1.3 Experimental Procedure

After some experimenting the stray light was reduced to a negligible level at the wavelength shifts larger than the base width of the instrumental profile centered at the ruby wavelength, i.e. larger than 16 Å. The plasma radiation was negligible too. The electronic noise was reduced to a sufficiently low level by eliminating ground loops and shielding the BNC cables. The scattered spectrum was taken shot to shot (from 3 to 6 points at each wavelength shift).

An oscillogram of the scattered pulse and the reference pulse is shown in Figure 5.5.

The results are given and discussed in Chapter 6.

# CHAPTER 6

# RESULTS AND DISCUSSION

## 6.1 Results

The results are divided into three sections: photographic study of the arc, radial electron density distribution and radial electron temperature distribution. The ion temperature and the radial pressure distribution are given in the subsection "Discussion."

### 6.1.1 Photographic Study of the Arc

The arc was photographed by the smear camera. The radial spread of the arc, its uniform rotation and its unstationary rotation were studied. A few smear photographs are shown in Figure 6.1.

*Radial Spread of the Arc.* The He II line is emitted from a region with a radius of 4-5 mm. The radius $r_0$ of the region from which mostly He I light is emitted slightly increases with the current. This variation is shown in the following table:

Figure 6.1 (following two pages)

Data: a), b), c) taken in full light; d), e), f), g), h) taken in the light of the He II 4686 Å line. B = 4.0 T on all pictures except c) where B = 2.5 T. Filling pressure: $p_f$ = 3 torr in all pictures, except h) where $p_f$ = 12 torr. 1 cm in the picture corresponds to 35.0 μsec. Plasma current: a), e), f), h), 2.8 kA; b) 2.0 kA; c) 3.4 kA; d) 4.7 kA; g) 3.4 kA. Smear camera slit-width is 0.5 mm for He II pictures and much narrower for full light pictures. Radial magnification is approximately 1.7.

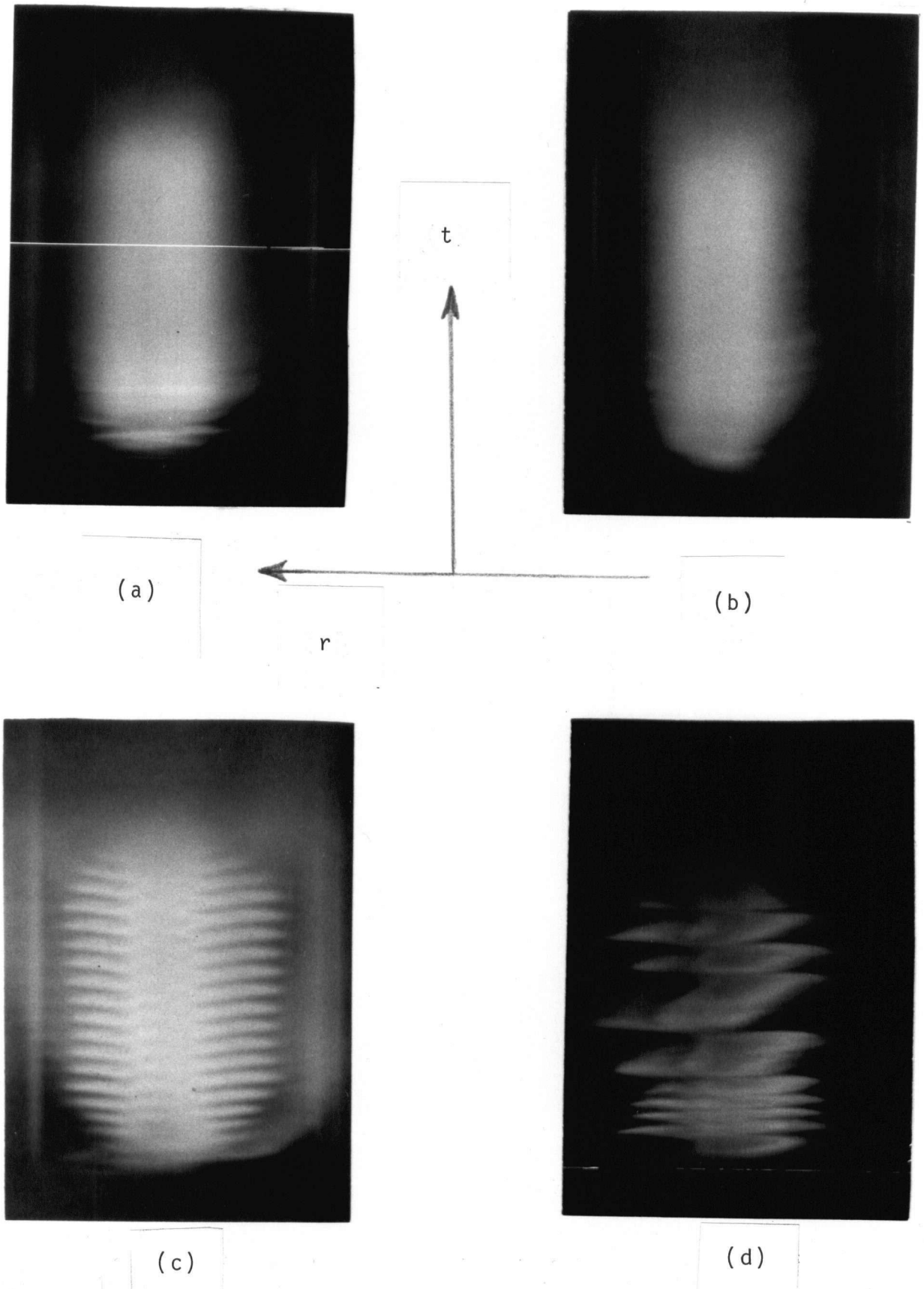


Figure 6.1 Smear pictures of the arc at varying values of the filling pressure $p_f$, plasma current, and magnetic field.

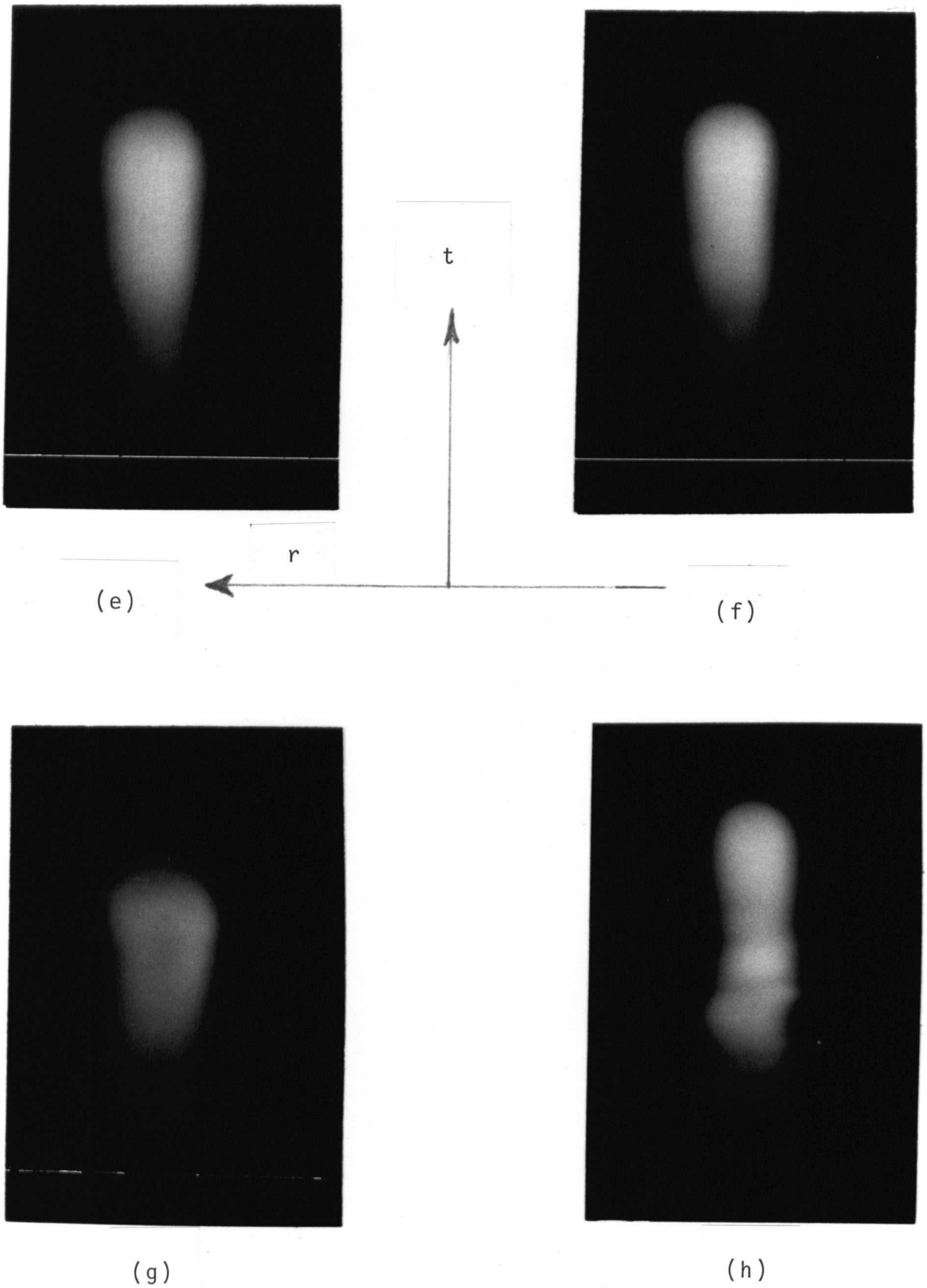


Figure 6.1 Smear pictures of the arc at varying values of the filling pressure $p_f$, plasma current, and magnetic field.

Figure 6.1A Unstationary arc in magnetic field. Data: $B_z$ = 4.0 T, $I_p$ = 4.5 kA, p = 3 torr. Radial magnification is 2.2 . Time: 1 cm corresponds to 27 μsec.

| Plasma current in kA | $r_0$ in mm |
|---|---|
| 2.0 | 7.0 |
| 2.7 | 8.0 |
| 3.4 | 11.0 - 12.0 |

For the plasma current of 3.4 kA the arc was unstationary. In all cases the arc kept well away from the discharge tube walls (the tube radius is 25 mm) and a discharge relatively free of impurities is expected.

*Uniform Rotation of the Arc*. The uniform rotation of the arc was studied with the smear camera and laser interferometry in the case of a slightly asymmetrical arc. It was found that the frequency of arc rotation varies with the radius and with the magnetic field. The results are shown in Figure 6.2. The measurements of the frequency of rotation were taken at 2 radii: at $r \simeq 4$ mm, i.e. at the radius of the arc on the He II 4686 Å photographs, and at $r \simeq 8$ mm, i.e. at the arc radius on the smear pictures taken in full light.

The azimuthal velocity $v_\phi$ can be calculated using the formula $v_\phi(r) = r\,\Omega(r)$, where $\Omega$ is the angular frequency of rotation. At a magnetic field of 4 Teslas the azimuthal arc velocity at radii of 4 mm and 8 mm is of the order of $10^4$ m $sec^{-1}$. A complete radial distribution of the azimuthal velocity cannot be given on the basis of the

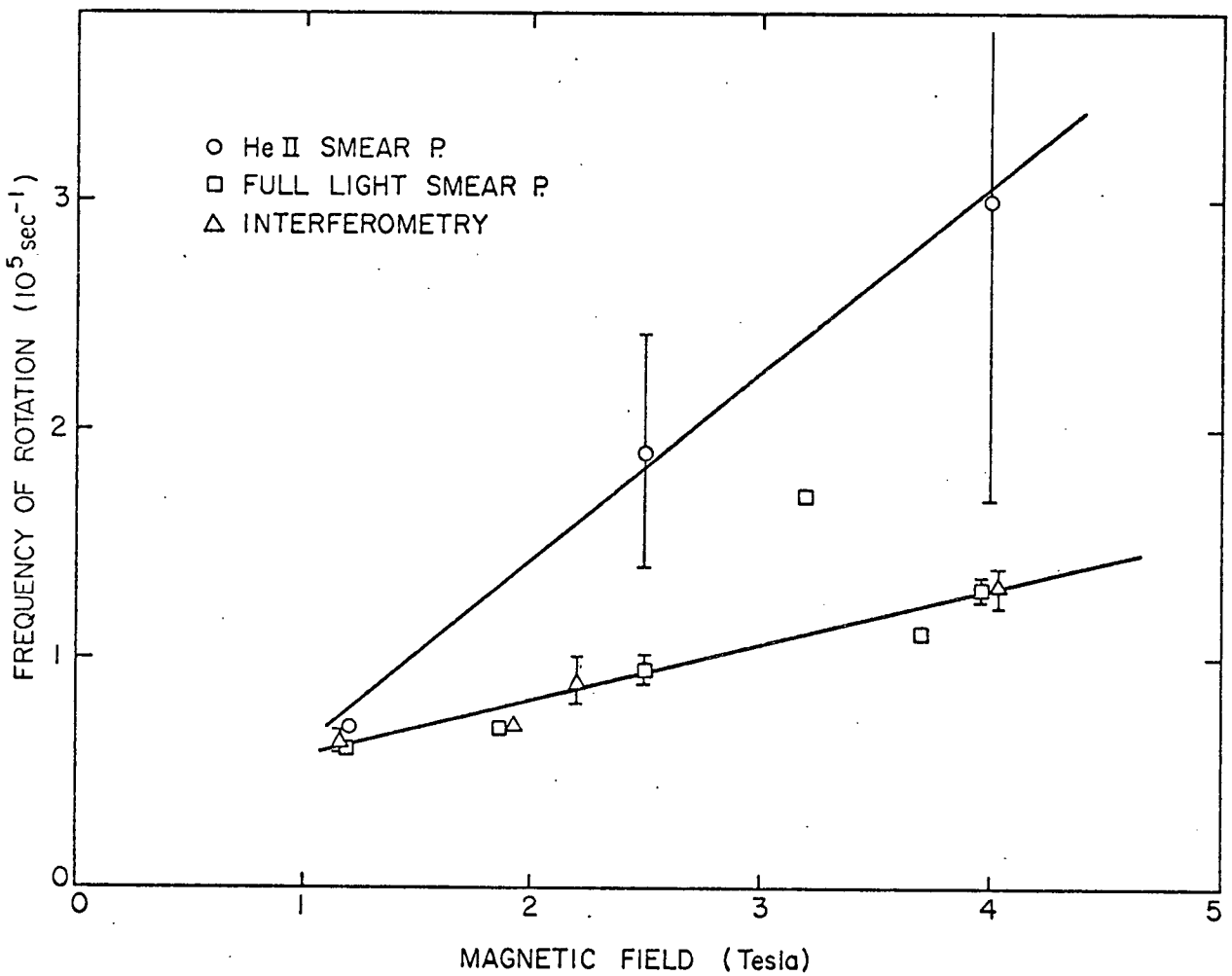


Figure 6.2 Frequency of arc rotation versus magnetic field.

measurements at two radii only. However, $v_\phi$ necessarily has to disappear at the arc axis and at the tube walls. For increasing radii, $v_\phi$ first increases, than reaches a maximum and decreases towards the tube walls. The rotation deviates from the rotation of a rigid body inasmuch as the viscosity influences the arc rotation.

*Unstationary Behaviour of the Arc.* A particularly useful result of the smear photography was the study of unstationary behaviour of the arc. In Chapter 1 it was mentioned that a stationary arc is not to be expected at high magnetic fields and high currents. This is in fact the case in this experiment. For the magnetic field of 4 Teslas and a pressure of 3 torr of He the maximum current at which the arc is still stationary is about 2.7 kA. This limit is lower if the discharge tube is not cleaned by pumping at least 5 minutes after each discharge.

A steady arc has been observed also at plasma currents above 2.7 kA, but the reproducibility of arc parameters was poor.

Increasing the magnetic field up to 4 T does not have a noticeable effect on the presence of the steady state of the plasma.

### 6.1.2 Radial Distribution of the Electron Density

The radial distribution of the electron density was measured by spectroscopy, laser interferometry and laser scattering.

The electron density obtained from the laser scattering data was determined simultaneously with the electron temperature by fitting the experimental scattering profile to the theoretical one. The fitting procedure is described in Chapter 5. The least square fitting was used. The scattering profile is shown in Figure 6.3.* The fitting yielded:

$$\alpha = (0.3 \pm 0.1)$$

and consequently

$$n_e = (1.1 \pm 0.7) \times 10^{16} \text{ cm}^{-3} .$$

The radial distribution of the electron density obtained from all three techniques is plotted on Figures 6.4 and 6.5. The matching of the spectroscopic and interferometric data was explained in Chapter 4, Section 4.3.1.

---

*One point of the scattered profile is far away from the theoretical profile indicating a possible anomaly of the scattered profile at a wavelength approximately corresponding to the plasma frequency. To make definite conclusions about the possible anomaly, more measurements would have to be taken at that wavelength. That part of the spectrum could be a subject of a future investigation. In the fitting of the theoretical profile on experimental data, that point was neglected.

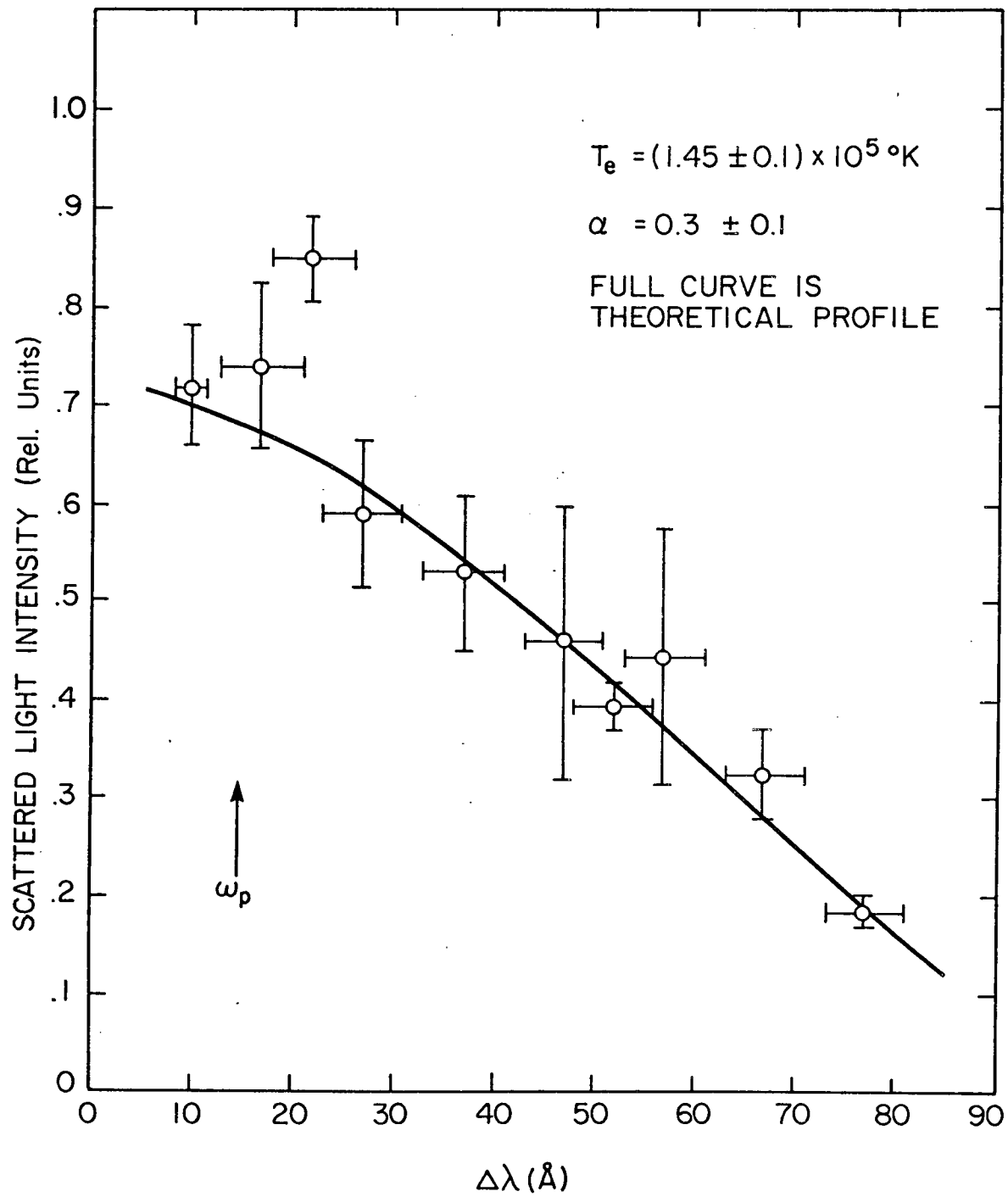


Figure 6.3 Laser scattering profile. Data: $B_z$=4.0 T, $I_p$=2.7 kA, $p_f$=3 torr, t=150 μsec.

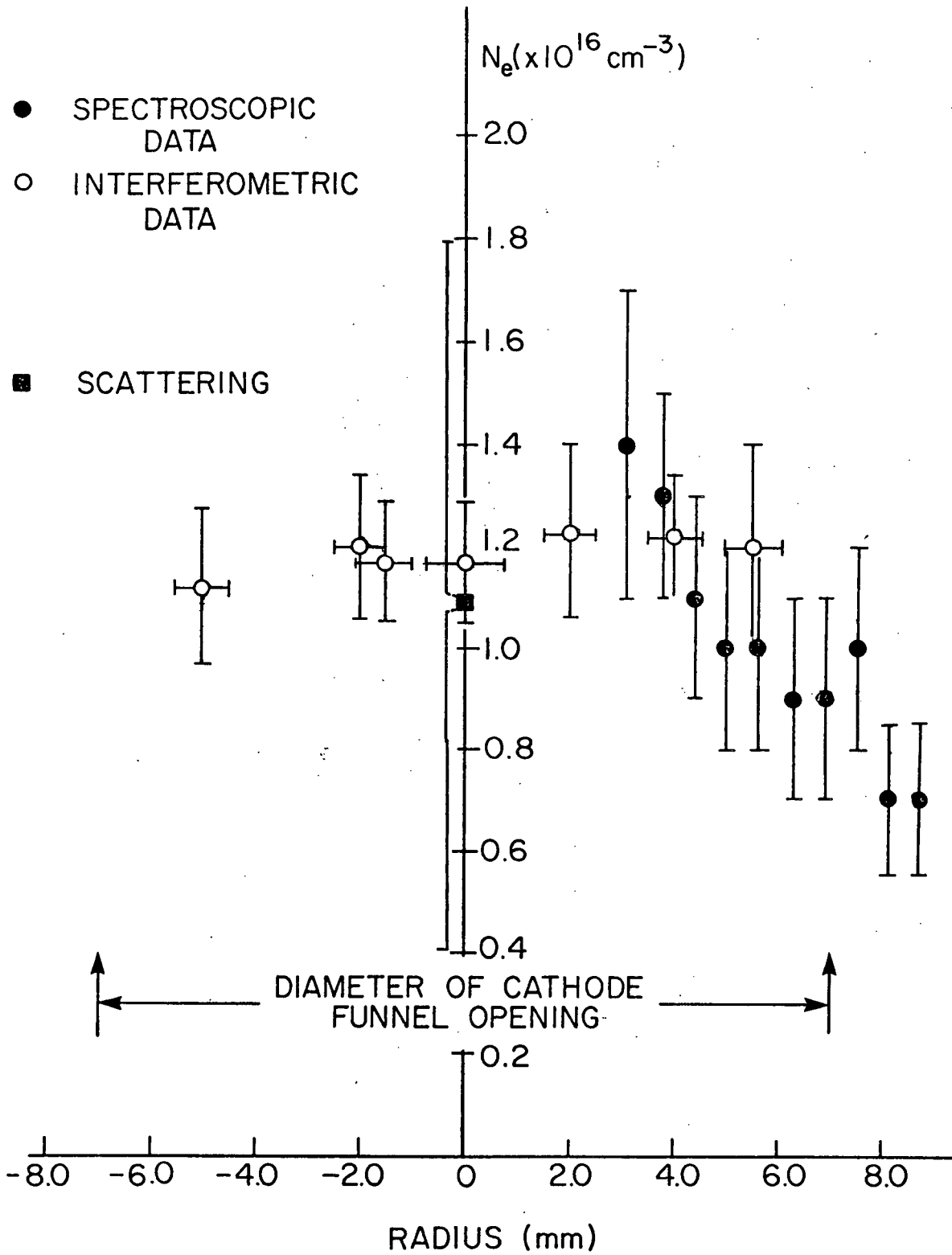


Figure 6.4 Radial electron density distribution in the arc. Data: $B_z$=4.0 T, $I_p$=2.7 kA, $p_f$=3 torr, t=150 μsec.

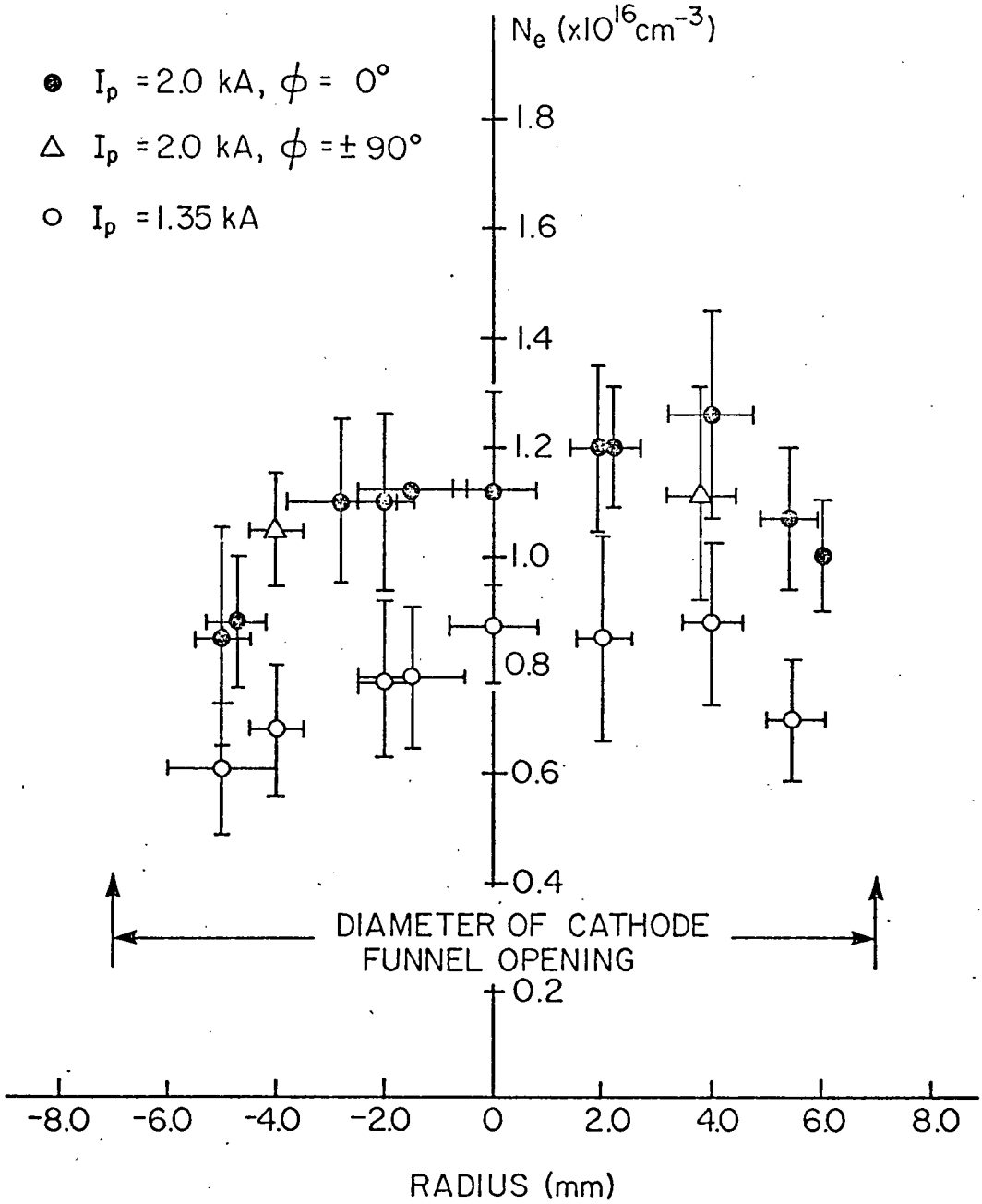


Figure 6.5 Radial electron density distribution in the arc. Data: $B_z$=4.0 T, $p_f$=3 torr, t=150 μsec.

The errors of interferometrically measured electron densities are between 15% and 30%, those of spectroscopically measured densities are from 20 - 30%.

### 6.1.3 Radial Distribution of Electron Temperature

The radial distribution of electron temperature was obtained from spectroscopy and laser scattering. Both methods complemented each other: spectroscopical measurements yielded the temperature in the cooler regions of the arc at radii 2.5 mm $< r \leq$ 5 mm; the laser scattering gave the axial arc temperature. The temperature distribution is plotted in Figure 6.6.

For the same set of plasma parameters two temperature curves were obtained from spectroscopic measurements: for one the Corona ratio of $n_2/n_1$ was used and for the other the ratio $n_2/n_1$ determined experimentally by Bergstedt [5]. The difference between the two curves arises because of a displacement of ionization due to arc dynamics (see Chapter 3, 3.1.3.2). The actual temperature distribution most likely lies close to the curve obtained from the experimental values of $n_2/n_1$.

The errors in temperature obtained from spectroscopic data are a combination of a statistical error from the average over 3 temperature profiles and the errors of each individual profile. The latter errors were estimated from the uncertainty

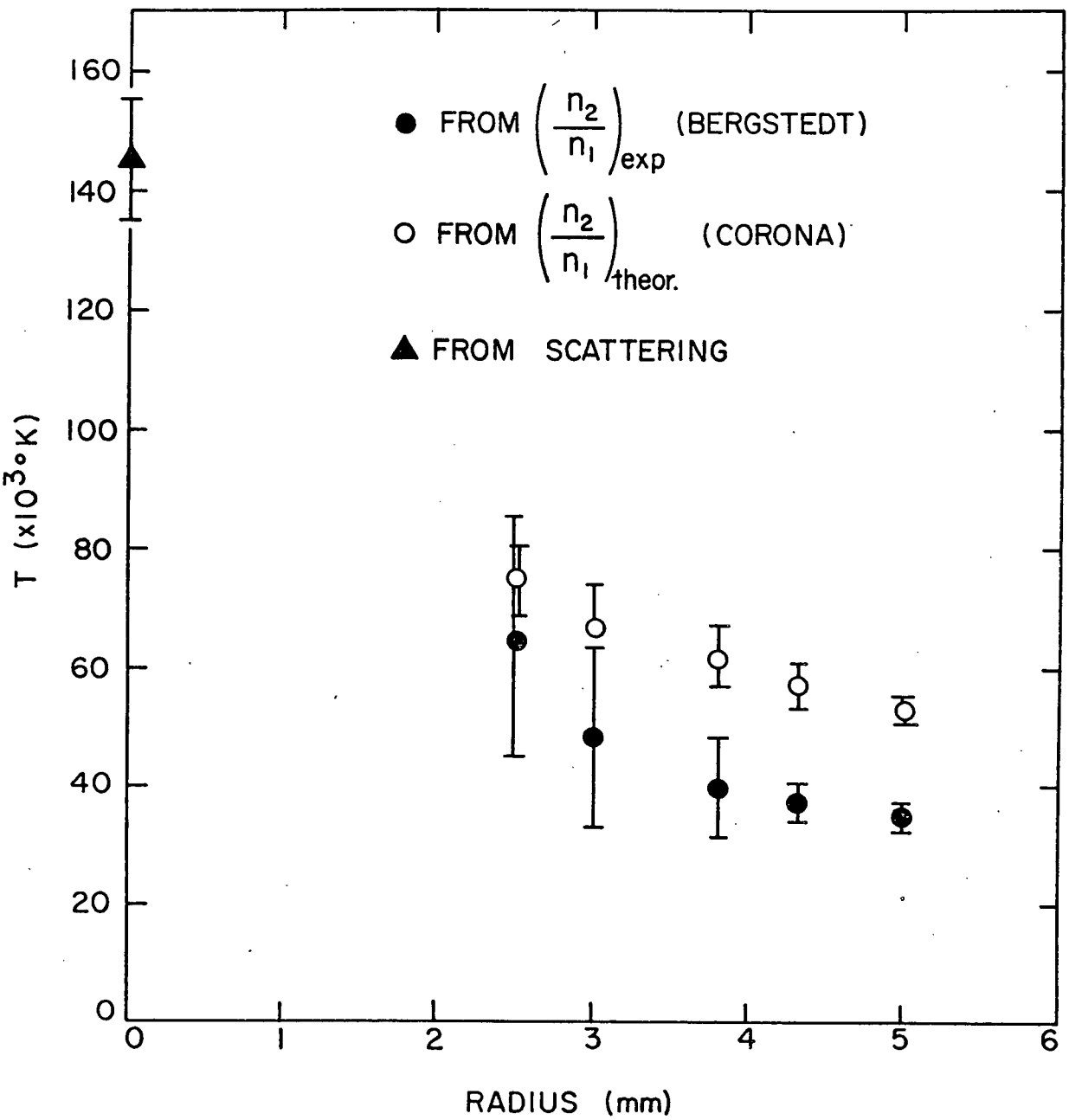


Figure 6.6 Radial temperature distribution in the arc. Data: $B_z$=4.0 T, $I_p$=2.7 kA, $p_f$=3 torr, t=150 μsec.

of the intensity ratio to a factor of 2. All temperature measurements are within an error of 30%.

The axial electron temperature at a plasma current of 2.7 kA is (145 ± 10) x $10^3$°K.

## 6.2 Discussion

The discussion is divided into the following subsections: the arc rotation, electron density distribution, electron temperature distribution, ion temperature and radial pressure distribution in the arc. The results are compared also with the theoretical predictions.

### 6.2.1 Arc Rotation

In Chapter 1 the arc rotation for a symmetrical configuration of the discharge system was described. It was pointed out that the current density component perpendicular to the magnetic field $j_\perp$ is positive at the anode funnel and negative at the cathode funnel. Consequently the arc rotates in one direction in the cathode region and in the other direction in the anode region. In the midplane between the electrodes (z = 0) the velocity $v_\phi$ is equal to zero.

A large observed velocity of rotation $v_\phi$ in the plane at z = 0 is due to the asymmetry of the electrode funnels. In Chapter 2 it was pointed out that the funnels

are made asymmetrical intentionally in order to provide a fast rotation of the whole arc and consequently assure a good rotational symmetry of the arc in the observation plane (at z = 0).

From Figure 2.2 it is evident that the anode funnel is wider and it ends in a lower magnetic field than the cathode funnel. As all the current has to flow into the cathode funnel also $j_\perp$ is greater at the cathode than at the anode funnel. The azimuthal force density ($-j_\perp B_m \vec{e}_\phi$) is therefore greater in the cathode than in the anode region; the whole arc rotation is determined by the cathode azimuthal force density. The speed of rotation decreases uniformly from the cathode funnel towards the anode funnel. The magnitude and axial distribution of the rotational velocity $v_\phi$ depends strongly on the geometry of the electrodes and funnels.

The calculation of the dependence of $v_\phi$ on the magnetic field and radius is beyond the scope of this thesis. Essentially the equation of motion (1.5) should be solved with $D(\eta\vec{v})$ and $\vec{j} \times \vec{B}$ as the most important terms [36]. The solution depends on ion viscosity $\eta_i(r)$, $j_r(r)$ and $B_z$. Unfortunately $j_r(r)$ is not known and rough approximations have to be used. Approximately a linear dependence on $B_z$ can be expected if $\omega_i \tau_{ii} << 1$ ($\omega_i$ = ion gyrofrequency, $\tau_{ii}$ = ion-ion collision time) which is the case in this experiment. The experimental data (Figure 6.2) confirm the linear dependence of $v_\phi$ on $B_z$.

### 6.2.2 Electron Density Distribution

The electron density profiles obtained from interferometric measurements indicate that the electron density is slightly inhomogeneous along the arc axis. If the homogeneity were to be assumed the plasma length would have to be 52 cm. The actual distance between the two end-on glass windows is 65 cm. A reasonable picture of the discharge is given by the model in which the electron density decreases from the center of the discharg ($z = 0$) towards the electrodes ($z = \pm L/2$).

As an example it will be shown that this variati is fairly small. For a similar discharge Grassman [4] has established experimentally that the axial electron density variations satisfied the inequality $\partial n_e/\partial z < n_e/3\ell$, where $\ell$ is the length of plasma below the magnetic field coil ($\ell = 50$ cm in his case, $\ell = 26$ cm in the experiment described in this report). If the same type of exponential decrease of electron density along the magnetic field is assumed here, the electron density would vary according to inequality:

$$\frac{\partial n_e}{\partial z} < \frac{1}{5}\frac{n_e}{\ell} \qquad (6.1)$$

The electron density at the ends of the magnetic field coils would thus be 20% smaller than at $z = 0$ and at

the electrodes 40% smaller than at z = 0. In fact the electron density probably decreases even slower below the magnetic field coils and faster closer to the electrodes.

For the discussion of the radial electron density distribution the reader is referred to the theoretical discussion of the Nernst effect in Chapter 1, section 1.1.1. According to theory, the electron density should be constant in regions where the Nernst effect is dominant.* The electron density measured in this experiment is constant within 4% for $r \leq 2$ mm and within 20% for $r \leq 4$ mm. As the errors of measurement are between 15% and 30%, the electron density can be considered constant for radii $r \leq 4$ mm. It can be concluded that the Nernst effect plays an important role in the arc for radii smaller than 2 to 4 mm.

The electron density profiles show a slight radial asymmetry (within 30% in the worst case). The asymmetry is likely due to two reasons: (1) a slight misalignment of the discharge axis with respect to the magnetic field axis and (2) nonuniform erosion of the

---

*In derivation of this result the ion temperature was assumed to be equal to the electron temperature. If the ion temperature is much smaller, the electron density might be a slight function of temperature [7]. However for helium the variation is within the experimental errors for the electron and ion temperature difference estimated in section 6.2.4.

discussion of the Nernst effect in Chapter 1, section 1.1.1. in regions where the Nernst effect is dominant.* The electron concluded that the Nernst effect plays an important role in

the electrodes, observed in this experiment. The arc misalignment might cause a bunching of the electron density towards one side of the discharge tube due to $\vec{E} \times \vec{B}$ forces.

### 6.2.3 Electron Temperature Distribution

The temperature distribution measured in this experiment is comparable to that obtained in similar arcs elsewhere [1-5]. The axial temperatures of over 200,000°K have been reported. These axial temperatures have been determined from spectroscopic measurements or extrapolations towards the axis from the temperature profiles measured in the cooler regions of the arc.

Laser scattering is, however, a more reliable method for the measurement of so high temperatures. Previous magnetically stablized arcs [1-5] were not designed for laser scattering experiments. The only scattering experiment reported on such arcs, giving an axial temperature of 40,000°K where a temperature of over 200,000°K had been estimated from spectroscopical data, was therefore unsuccessful.

As the arc in this experiment was designed for laser scattering experiments it was natural to measure the axial arc temperature by this method. The axial temperature in this arc (145,000°K) is in good agreement

with the axial arc temperatures in references [1-5]. It has to be noted that the magnetic field in this experiment was 4 Teslas and 5 or 6 Teslas in the previously reported experiments. The size of the whole apparatus (due to smaller available energy) was also smaller and the plasma currents were different in this experiment. The comparison of the data is therefore somehow difficult.

### 6.2.4 Ion Temperature

The ion temperature of the arc has not been measured. In spite of that some knowledge about it can be obtained by evaluating the criteria for the equality of ion and electron temperature. The two temperatures can be different due to two main reasons: finite electron-ion energy transfer time and radial temperature gradients.

*Transfer of Energy from the Electrons to the Ions*. In the electric arc the electrons gain their energy from the electric current by Ohmic heating. Part of this energy is transferred to the ions, part of it is lost in other processes. The energy balance can be expressed with the following inequality:

$$\frac{j_z^2}{\sigma_{\parallel}^2} > \frac{n_e}{\tau_e}\frac{m_e}{m_i}\, 3\, K(T_e - T_i) \qquad (6.2)$$

where $\tau_e$ = electron ion collision time defined in Chapter 1.

The term on the left-hand side of the inequality (6.2) is the ohmic heat generated in the electron gas per unit volume and second. The term on the right-hand side is the heat per unit volume and second transferred from the electrons to the ions.

The electric current density can be estimated by noting that approximately 80% of all the current flows within the distinguished flux tube [3]. The electron and ion temperature difference will be estimated on the discharge axis at the midplane between the electrodes (z = 0) and for a plasma current of 2.7 kA. At z = 0 the distinguished flux tube has a radius of 0.4 cm, therefore

$$j_z \simeq 4 \times 10^3 \text{ A/cm}^2$$

For $n_e = 1.2 \times 10^{16} \text{cm}^{-3}$ and $m_i = m_{He} = 6.7 \times 10^{-27}$ kg the temperature difference is:

$$T_e - T_i < 40{,}000°\text{K}$$

The result shows that the electron and ion temperatures are approximately equal.

*Temperature Difference Due to Temperature Gradients.* The arc is strongly inhomogeneous in the radial direction and is

dominated by dynamic processes. For the electron temperature to be equal to the ion temperature it is necessary that the spatial variation of the electron temperature should be small over the distances the ions travel in times of the order of the electron ion equilibration time $\tau_{eq}$ [15].

In the arc discussed here the ion flow is parallel to the temperature gradient. The condition for the equality of electron and ion temperature is

$$\frac{\nabla_r T_e}{T_e} v_{2r} \tau_{eq} << 1 \qquad (6.3)$$

The temperature gradients in this arc are large: $\nabla_r T_e/T_e \simeq 2\ cm^{-1}$. $\tau_{eq} \simeq 0.1$ μsec for He at the temperature of 140.000°K. Then $v_r$ has to satisfy the inequality $v_{2r} << 5 \times 10^4\ m/sec^{-1}$. In this arc the ion velocity $v_{2r}$ is about 10 - 20 m $sec^{-1}$. The condition (6.3) is satisfied and it can be concluded that the electron and ion temperature are approximately equal.

### 6.2.5 Pressure Distribution

In Chapter 1 the fundamental importance of the pressure increase in an arc in magnetic field was discussed. In this section the radial pressure distribution will be

calculated from the experimental values of electron density and temperature.

The total pressure in the arc is the sum of partial pressures of the electrons, neutral atoms and once and twice charged helium ions:

$$p(r) = [n_e(r) + n_0(r) + n_1(r) + n_2(r)]\, KT(r) \qquad (6.4)$$

where:

$p(r)$ = total local pressure,

$n_0(r)$, $n_1(r)$, $n_2(r)$, $n_e(r)$ are the local densities of neutrals, once and twice charged ions and electrons respectively.

The density of once and twice charged helium ions are expressed in terms of the electron density $n_e$ and the ratio $n_2/n_1$ with the help of quasineutrality condition. In the region where both species of ions are present and no neutrals one gets:

$$n_e = n_1 + 2n_2 \qquad (6.5)$$

and

$$n_1(r) = \frac{1}{1 + 2\,\frac{n_2}{n_1}(r)} \quad , \quad n_2 = \frac{\frac{n_2}{n_1}(r)}{1 + 2\,\frac{n_2}{n_1}(r)} \qquad (6.6)$$

At the arc axis the plasma is fully ionized and one may write $n_e(0) = 2\, n_2(0)$.

The ratio $\frac{n_2}{n_1}$ (r) was calculated from the temperature distribution and from $\frac{n_2}{n_1}$ (T) measured by Bergstedt [5]. The problem of calculating the density ratio of once charged helium ions and neutral atoms is even greater than that of finding the ratio $n_2/n_1$. An experimental value for $n_0/n_1$ obtained by Bergstedt [37] was used here to give an order of magnitude of the partial pressure of neutral helium.

The pressure distribution is shown in Figure 6.7. The errors in pressure are between 30% and 50%, because the electron density and temperature errors were between 15% and 30%.

The experimental results prove that the pressure increase is substantial inside the hot core of the arc.

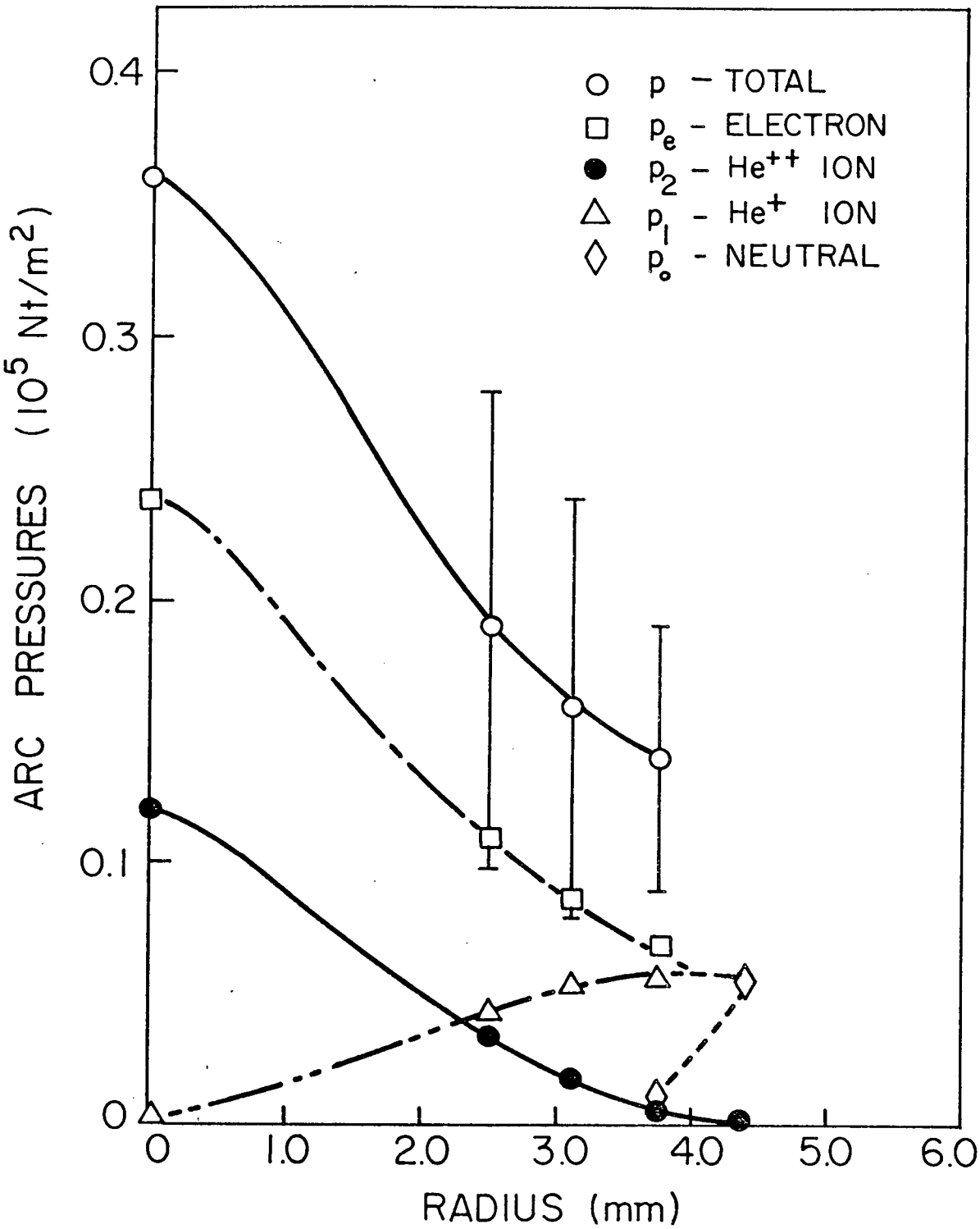


Figure 6.7 Radial distribution of total and partial pressures in the arc. Data: $B_z$=4.0 T, $I_p$=2.7 kA, $p_f$=3 torr, t=150 μsec.

# CHAPTER 7

# SUMMARY AND CONCLUSIONS

The aim of the work reported in this thesis was to build a magnetically stabilized helium arc for scattering experiments and to measure the arc parameters. The thesis describes the details of the design of the apparatus and the measurement of plasma parameters.

The main features of the apparatus are:
(1) Ports in the discharge tube at the center of the coil configuration, suitable for conducting laser scattering experiments in the plane perpendicular to the magnetic field and (2) Relatively small energy used for the production of the magnetic field and the plasma.

The apparatus has performed well and is reliable also for future work.

The arc was studied with a variety of techniques: time resolved photography and spectroscopy, laser interferometry and laser scattering. The measurements indicate that the arc is stable and approximately rotationally symmetric at currents up to 2.7 kA, at a filling pressure of 3 torr and a magnetic field of 4 Teslas (in the middle of the discharge at $z = 0$).

From spectroscopic data the electron density, temperature and pressure were obtained in the cooler regions of the discharge.

As the spectroscopic measurements are difficult and unreliable at temperatures above 100,000 °K, laser interferometry and laser scattering were used for the measurement of electron density and temperature at the arc axis. Laser interferometry and laser scattering were used successfully for the first time on a magnetically stabilized arc. An axial arc temperature of about 150,000 °K was obtained. The electron density is about $1.2 \times 10^{16}$ $cm^{-3}$ and is approximately constant in the hot core of the arc.

The following table gives a comparison between the arc designed in this experiment and the arcs reported previously [1-5]: (p. 114).

Thus the measurements show a high axial temperature a constant electron density in the hot core of the arc, and a substantial pressure increase at the arc axis as predicted by theory.

Now the plasma properties are known and a number of laser scattering studies can be conducted in this arc.

1. Measurement of electron density and temperature at different radii to get the whole radial profile from scattering data. Different plasma currents can also be used (e.g. 2.0 kA and 3.4 kA).

TABLE 1

COMPARISON OF THE MOST IMPORTANT PARAMETERS OF THE APPARATUS REPORTED IN THIS THESIS AND IN REFERENCES [1-7]

| Energy of the Magnetic Field Capacitor Bank* | Energy of the Plasma Capacitor Bank* | $B_z$ at $z=0$** | Plasma Current** | Axial $n_e$ | Axial $T_e$ | Axial Total Pressure | Reference |
|---|---|---|---|---|---|---|---|
| kJ | kJ | Tesla | kA | $\times 10^{16}$ $cm^{-3}$ | $\times 10^{5}$ °K | $Nt/m^2$ | |
| 29 | 25 | 4.0 | 2.7 | 1.2 | 1.45 | 0.36 | This thesis |
| 100 | 100 | 5.5-8.0 | -*** | - | >2.0 | - | [1] |
| 100 | 50 | 6.0 | 2.6 | 1.0-2.0 | >2.0 | - | [2] |
| - | - | 6.0 | 2.6 | 1.5 | 4.0 | ≃1.0 | [4] |
| 100 | 50 | 4.8 | 3.8 | 1.1 | 2.0 | 0.44 | [5] |
| 450 | 50 | 8.0 | 2.1 | 0.8 | 2.5 | - | [7]**** |

*Maximum stored energy (at rated voltage)

**Values at which the parameters were measured

***Horizontal bar means that no data were available

****Filling gas is hydrogen.

Thus the influence of the temperature and pressure gradients on the thermal equilibrium can be determined.

2. The modulation of the scattered profiles by the magnetic field can be studied.

3. The density fluctuations can be studied in the presence of large temperature gradients.

# REFERENCES


[1] WULFF, H. Production and behaviour of a magnetically stabilized high-density high-temperature plasma. Proc. VII$^{th}$ Int. Conf. on Phenomena in Ionized Gasses, Beograd, 1965.

[2] KLÜBER, O. Untersuchung des Druckaufbaus einer stationären, magnetfeldstabilisierten Helium-Entladung mit Hilfe magnetischer Messungen. Z. Naturforsch. 22a, 1599-1612 (1967).

[3] KLÜBER, O. Untersuchungen zur Stromdichteverteilung eines Lichtbogens im Magnetfeld. Z. Naturforsch. 24a, 1473-1491 (1969).

[4] GRASSMANN, P.H. Der Druckaufbau in einem stationären, magnetfeldstabilisierten Heliumplasma hoher Dichte und Temperatur. Z. Naturforsch. 23a, 251-263 (1968).

[5] BERGSTEDT, K. Die Beeinflussung des Ionisationsgrades durch Diffusion - und Massenströme im Plasma. Z. Naturforsch. 24a, 299-319 (1969).

[6] MAECKER, H. Über die Charakteristiken zylindrischer Bögen. Z. Phys. 157. 1-29 (1959).

[7] VENUS, G. Elektronendichteverlauf in magnetisierten Wasserstoffbögen bei Abweichung der Ionentemperatur von der Elektronentemperatur. Z. Phys. 259, 437-450 (1973).

[8] NEUFELD, C.R. Phys. Letters 31A (1969), 19.

[9] SHKAROFSKY, I.P., JONSTON, T.W., BACHYNSKI, M.P. The Particle Kinetics of Plasmas, Addison-Wesley 1966, p. 259.

[10] BRAGINSKII, S.I. Transport processes in a plasma. Reviews of Plasma Physics, vol. 1, Consultants Bureau, N.Y., 1965.

[11] WIENECKE, R. Druckerhöhung in der zylindersymmetrischen Lichtbogensäule bei überlagertem axialen Magnetfeld. Z. Naturforsch, 18a (1963), p. 1151-1156.

[12] D.H. PARKINSON, B.E. MULLHALL. The Generation of High Magnetic Fields. Plenum Press, 1967.

[13] H. KNÖPFEL. Pulsed High Magnetic Fields. North Holland, 1970.

[14] M.L. DALTON, Jr. Determination of Line-Widths by Slit-Width Alterations. Appl. Optics, vol. 4 (1965), 603.

[15] H.R. GRIEM. Plasma Spectroscopy. McGraw Hill, 1964.

[16] W.L. BARR. Method for Computing the Radial Distribution of Emitters in a Cylindrical Source. J. Opt. Soc. A. vol 52 (1962), 885.

[17] A.J. BARNARD, J. COOPER, L.J. SHAMEY (RCS). The broadening of He I 4471 Å and its forbidden components. Astron. and Astrophysics 1: 28-36.

[18] A.J. BARNARD, R.H. NELSON. Profiles of He I 4471 Å and 4922 angstroms in a pulsed arc. T. Quant. Spectrosc. and Radiot. Transfer (GB) 11, No. 3, 161-7.

[19] D.C. STEVENSON. Measurement of the profile of He I 4471 A at low electron densities. M.Sc. Thesis, University of British Columbia, 1973.

[20] D.D. BURGESS, J.E. JENKINS. Experimental studies of helium line broadening in a plasma: I. High electron densities. J. Phys. B: Atom. Molec. Phys. 4, (1971), 1353-63.

D.D. BURGESS, CAIRNS, C.J. Experimental studies of helium line broadening in plasma: II Low electron densities (lines with forbidden components) J. Phys. B: Atom. Molec.Phys. 4, 1364-76 (1971).

[21] C. DEUTSCH et al. Effects Stark et Zeeman combinés sur les transitions hydrogenoïdes de l'helium neutre. J.Q.S.R.T. vol. 8, 1027-1059.

[22] C. DUTSCH. Influence of a Strong Magnetic Field on Plasma-Broadened 2P-42(Q=P,D,F) He I Lines. Phys. Rev. A. vol. 2, 1258.

[23] C. MAHN. Über das unterschiedliche Ionisationsgleichgewicht wasserstoff- und alkali-ähnlicher Ionen in Optisch dünnen Plasmen. Z. Naturforsch 22a, 1939-1952 (1967).

[24] R. MEWE. Relative intensity of helium spectral lines as a function of electron temperature and density. Brit. J. Appl. Phys. vol. 18, p. 107 (1967).

[25] TICHMANN, K. Einfluss von Relaxationserscheinungen etc., Internal Report, Institut für Plasmaphysik, IPP 2/77, 1968.

[26] HUNI, J.P.R. Cylindrical Imploding Detonations.Ph.D. thesis, University of British Columbia, 1970.

[27] NULL, M., LOUZIER, W. J. Opt. Soc. Am. 52 (1962), p. 1156. Carbon arc as a radiation standard.

[28] BERG, W.F. Photographic Aspects of High Speed Photography - Kurzzeitphotographie, VII. Internationaler Kongress, Zürich, 1965.

[29] TODD, H.N.,ZAKIA, R.D. Photographic Sensitometry. Morgan & Morgan, N.Y., 1969.

[30] FUNK, L.W. A high performance laser-excited interferometer for measuring electron densities. Ph.D. Thesis, University of British Columbia, 1971.

[31] PRESTON, J.M., CURZON, F.L. The performance of a high frequency interferometer for direct recording of electron densities. J. Phys. E: Sci. Instrum. (1973), vol. 6 (to be published).

[32] EVANS, D.E. and KATZENSTEIN, J. Laser light scattering in laboratory plasmas. Rep. Prog. Phys., 1969, 32, 207-271.

[33] KEGEL, W.H. Internal Report. Institut für Plasmaphysik, Garching, IPP 6/34, 1965.

[34] CHURCHLAND, M.T. Enhancements observed in the scattered light spectra of a carbon arc plasma. Ph.D. Thesis, The University of British Columbia, 1972.

[35] GODFREY, L. M.Sc. Thesis, The University of British Columbia, 1973.

[36] MAHN, C., RINGLER, H., ZANKL, G. Experimentelle Untersuchungen an einem Wasserstoff-Lichtbogen im achsenparallelen Magnetfeld. Internal report. Institut für Plasmaphysik, Garching, IPP 3/44, 1966.

[37] BERGSTEDT, K. Über die Verschleppung der Ionisation in Plasma durch Teilchenströme in Richtung eines Temperaturgradienten. Internal Report, Institut für Plasmaphysik, Garching, IPP 3/64, 1967.

# APPENDIX A

## GENERALIZED OHM'S LAW

As it is conventionally stated Ohm's law $\vec{j} = \sigma\vec{E}$ relates the current density to the electric field at a given instant of time. However, the electric field is actually responsible for the acceleration of the electrons rather than their velocity so that in the general case a more complicated relationship between $\vec{j}$ and $\vec{E}$ is obtained. Generalized Ohm's law will be derived in this Appendix.

For a two component plasma the equations of motion are:

$$m_e n_e \frac{d\vec{v}_e}{dt} + \nabla p_e = -e\, n_e(\vec{E} + \vec{v}_e \times \vec{B}) + \vec{R}_{ei} \qquad (A.1)$$

$$m_i n_i \frac{d\vec{v}_i}{dt} + \nabla p_i = Ze\, n_i(\vec{E} + \vec{v}_i \times \vec{B}) + \vec{R}_{ie} \qquad (A.1a)$$

where the indices e and i relate the quantities to the electrons and ions respectively. $\vec{R}_{ei} = -\vec{R}_{ie}$ is the friction force between the electrons and ions (the transfer of momentum from ions to electrons by collisions).

If the equations (A.1) are divided by their respective mass density and subtracted from each other the following equation is obtained for a stationary state:

$$\frac{1}{en_e}\vec{R}_{ei} = \vec{E} + (\vec{v} + \vec{u}) \times \vec{B} + \frac{1}{en_e}\nabla p_e \qquad (A.2)$$

where $\vec{u} = \vec{v}_e - \vec{v}_i = -\frac{1}{en_e}\vec{j}$ , and

$\vec{v}$ = center of mass velocity.

To obtain the equation (A.2) the following assumptions were made: $m_e/m_i << 1$, $\nabla p_i/\rho_i << \nabla p_e/\rho_e$ .

The derivation for a three component plasma is similar but more complicated. The result are two additional terms in equation (A.2). One describes the diffusion of heavy particles and is given in equation (1.6) of Chapter 1 as term $\vec{d}$. The other term gives the electric field due to partial pressure gradients of heavy particles. It was neglected in equation (1.6) because it is not important for discussion in this report.

The transfer of momentum from ions to electrons by collisions is made up of two parts: the force of friction $\vec{R}_u$ (henceforth $\vec{R}_{ei} \equiv \vec{R}$) due to the existence of a relative velocity $\vec{u}$, and a thermal force $\vec{R}_T$, which arises by virtue of a gradient in the electron temperature. One can write in general

$$\vec{R} = \vec{R}_u + \vec{R}_T \qquad (A.3)$$

with

$$\vec{R}_u = \beta_{\parallel}\vec{u}_{\parallel} + \beta_{\perp}\vec{u}_{\perp} + \beta_x\vec{u} \times \vec{B} \qquad (A.4)$$

$$\vec{R}_T = \gamma_{\parallel}\nabla_{\parallel} + \gamma_{\perp}\nabla_{\perp}T + \gamma_x\nabla T \times \frac{\vec{B}}{B} \qquad (A.5)$$

In equations (A.4) and (A.5) the indices $\parallel$ and $\perp$ denote the components parallel and perpendicular to the magnetic field $\vec{B}$. The coefficients $\beta$ and $\gamma$ have been calculated from the plasma kinetic theory by Braginskii [10].

The friction force $\vec{R}_u$ can be expressed with the electric current density and conductivity in the form:

$$\vec{R}_u = en_e \left(\frac{\vec{j}_{\parallel}}{\sigma_{\parallel}} + \frac{\vec{j}_{\perp}}{\sigma_{\perp}}\right) \qquad (A.6)$$

The third term in equation (A.4) is small for large magnetic fields ($\omega_e\tau_e >> 1$), therefore it is not included in equation (A.6).

Inserting equation (A.3) with (A.5) and (A.6) into equation (A.2) generalized Ohm's law (equation (1.6)) is obtained for a two component plasma ($\vec{d} = 0$).

# APPENDIX B

## RADIAL MASS CURRENTS IN THE ARC

A complete derivation of radial mass currents in the arc will not be given because of the tedious algebra. For a more complete derivation the reader is referred to Bergstedt's derivation [37].

In the calculation of the radial velocities for a 3 component plasma 3 equations of motion are used: Equation (A.1) for the electrons, equation (A.1a) for singly charged ions (Z = 1), and an equation similar to (A.1a) for doubly ionized helium.

The center of mass velocities of the electrons $\vec{v}_e$, singly charged ions $\vec{v}_1$, and doubly charged ions $\vec{v}_2$ will be expressed with a linear combination of the center of mass velocity of the plasma $\vec{v}$, electric current $\vec{j}$ and a diffusion variable $\vec{d}$. These variables are defined with the following equations:

$$\vec{v} = \frac{m_{He}(n_1\vec{v}_1 + n_2\vec{v}_2) + m_e n_e \vec{v}_e}{m_{He}(n_1 + n_2) + m_e n_e} \quad , \tag{B.1}$$

$$\vec{j} = e(n_1\vec{v}_1 + 2n_2\vec{v}_2 - n_e\vec{v}_e) \quad , \tag{B.2}$$

$$\vec{d} = \frac{n_1 n_2}{(n_1 + n_2) n_e} (\vec{v}_2 - \vec{v}_1) \quad . \tag{B.3}$$

From these equations the center of mass velocities of the electrons and ions are obtained:

$$\vec{v}_2 = \vec{v} - \frac{n_1 + n_2}{A\, n_e} \frac{\vec{j}}{e} + \frac{n_1 + n_2}{A} \vec{d} \quad , \tag{B.4}$$

$$\vec{v}_1 = \vec{v} + \frac{\beta}{A} \frac{\vec{j}}{e} - \frac{n_e (n_1 + n_2)}{n_1 A} (1 + 2\beta) \vec{d}, \tag{B.5}$$

$$\vec{v}_2 = \vec{v} + \frac{\beta}{A} \frac{\vec{j}}{e} + \frac{n_e (n_1 + n_2)}{n_2 A} (1 + \beta) \vec{d} \quad , \tag{B.6}$$

where $\beta = m_e/m_{He} << 1$ and $A = n_1 + n_2 + \beta n_e$. With $\beta = 0$, the quasineutrality condition $n_e = n_1 + 2n_2$ and $j_r = 0$, one may write for the radial components of the C.M. velocities:

$$v_{er} = v_r + d_r \quad , \tag{B.7}$$

$$v_{1r} = v_r - \frac{n_e}{n_1} d_r \quad , \tag{B.8}$$

$$v_{2r} = v_r + \frac{n_e}{n_2} d_r \quad . \tag{B.9}$$

The equations (B.4), (B.5), and (B.6) have to be inserted into the equations of motion of plasma species (3 vector equations). The equation of motion of all the

plasma (equation 1.16 without the inertial terms) has to be also included.

With the assumptions: $v_{ez} B_\phi << v_{e\phi} B_z$, $j_z B_\phi << j_\phi B_z$, and $v_{2z} B_\phi << v_{2\phi} B_z$, the r- and $\phi$- components of the equation of motion together with the equation $j_r = 0$ one obtains a system of seven coupled equations. The unknowns in these equations are: the electric field $E_r$ and r- and $\phi$- components of $\vec{v}$, $\vec{j}$ and $\vec{d}$. Solving these equation one obtains $v_r$ and $d_r$ in terms of the measured variables. The ion velocities are then obtained from equations (B.8) and (B.9).

The result for $v_r$, taken from [37], is:

$$V_r = \frac{\varepsilon_{21}}{4(eB)^2 + (n_e \varepsilon_{21})^2} \{\frac{1}{eB} \frac{n_e \varepsilon_{21}}{\omega_e \tau_e} [1.2\, n_e K \nabla_r T - \nabla_r p]$$

$$+ 2 \frac{n_2}{n_1 + n_2} \nabla_r p_e + \frac{n_e}{n_1 + n_2} \nabla_r p_2\} , \qquad (B.10)$$

where $\varepsilon_{21}$ is friction coefficient between singly and doubly charged helium ions. It is defined by the equation:

$$\varepsilon_{21} = \frac{4}{3} \sqrt{2\pi \frac{m_2 m_1}{m_2 + m_1}} \left(\frac{Z_2 Z_1 e^2}{4\pi\varepsilon_0}\right)^2 \frac{\ell n \Lambda}{(KT)^{3/2}} \qquad (B.11)$$

$\ell n \Lambda$ is the Coulomb logarithm.

# APPENDIX C

## INTENSITY RATIO OF THE LINES He II 4686 Å AND He I 4471 Å

The radiated power per unit volume and unit solid angle in a transition from level p to level q is

$$i_{pq} = \frac{1}{4\pi} A_{pq} \frac{hc}{\lambda_{pq}} n_p \qquad (C.1)$$

where:

$A_{pq}$ = transition probability

$\lambda_{pq}$ = wavelength of the transition

$n_p$ = population density of the upper level of the transition.

The ratio of intensities of two spectral lines of Z-1 times and Z-2 times charged ions of the same element is

$$\frac{i_{pq}}{i_{rs}} = \frac{A_{pq}}{A_{rs}} \frac{\lambda_{rs}}{\lambda_{pq}} \frac{n_p^{(Z-1)}}{n_r^{(Z-2)}} \qquad (C.2)$$

For the electron density of about $10^{16} cm^{-3}$ the He I and He II levels are thermally populated for all the levels with principal quantum number $p \geq 4$ [e.g. 24]. When the levels are thermally populated their equilibrium

population density is given by Saha-Boltzmann equation:

$$\frac{n_e n_Z}{n_p^{(Z-1)}} = \frac{2Z_Z}{g_p^{(Z-1)}} \left(\frac{2\pi\, m_e\, KT_e}{h^2}\right)^{3/2} \exp\left\{-\frac{E_i^{(Z)} - E_p^{(Z-1)}}{KT_e}\right\} \tag{C.3}$$

Using equation (A.3) the ratio $n_p^{(Z-1)}/n_r^{(Z-2)}$ in equation (C.2) can be expressed with the ratio of ion densities of two successive ionization stages.

$$\frac{n_p^{(Z-1)}}{n_r^{(Z-2)}} = \frac{Z_{Z-1}}{Z_Z} \frac{g_p^{(Z-1)}}{g_r^{(Z-2)}} \exp\left\{-\frac{E_i^{(Z-1)} + E_r^{(Z-2)} + E_i^{(Z)} - E_p^{(Z-1)}}{KT_e}\right\} \times \frac{n_Z}{n_{Z-1}} \tag{C.4}$$

$$\frac{n_p^{(Z-1)}}{n_r^{(Z-2)}} = f(T_e)\, \frac{n_Z}{n_{Z-1}} \tag{C.5}$$

In equations (C.3) to (C.5) the symbols have the following meaning:

$n_e$ is the electron density.

$n_p^{(Z-1)}$, $g_p^{(Z-1)}$, $E_p^{(Z-1)}$, $n_r^{(Z-2)}$, $g_r^{(Z-2)}$ $E_r^{(Z-2)}$ are the

population densities, statistical weights and energies of the upper levels of Z-1 and Z-2 times charged ions.

$Z_Z$, $E_i^{(Z)}$, $Z_{Z-1}$, $E_i^{(Z-1)}$ are the partition functions and ionization energies of Z and Z-1 times charged ions. $f(T_e)$ is a function of temperature only and tabulated atomic constants.

Combining equations (C.2) an (C.5) the line intensity ratio becomes:

$$\frac{i_{pq}}{i_{rs}} = \frac{A_{pq}}{A_{rs}} \frac{\lambda_{rs}}{\lambda_{pq}} f(T_e) \frac{n_z}{n_{Z-1}} \qquad (C.6)$$

This result is used in Chapter 3.